Multifunctional Reflectionless Metasurfaces

Amr Elsakka

School of Electrical Engineering

Thesis submitted for examination for the degree of Master of Science in Technology.

Espoo 18.04.2016

Thesis supervisor:

Prof. Sergei Tretyakov

Thesis advisor:

MSc Viktar Asadchy

Aalto University
School of Electrical
Engineering

AALTO UNIVERSITY
SCHOOL OF ELECTRICAL ENGINEERING

ABSTRACT OF THE
MASTER'S THESIS

Author: Amr Elsakka

Title: Multifunctional Reflectionless Metasurfaces

Date: 18.04.2016 Language: English Number of pages: 7+36

Department of Radio Science and Technology

Professorship: Radio Science

Supervisor: Prof. Sergei Tretyakov

Advisor: MSc Viktar Asadchy

Engineering reflection and transmission of electromagnetic waves is very important in a wide range of applications; that is why there is always a continuous need for new solutions that are more efficient and flexible. Here, design and realization of a single-layer meta-transmitarray (metasurface) which provides a certain functionality in a narrow frequency band while remains reflectionless (transparent) outside of the operational frequency band is presented. Metasurfaces are structures that represent composites comprising two-dimensional arrays of electrically small elements that are electrically and magnetically polarizable. Realizing such transmitarrays would allow integrating several metasurfaces in composite structures that perform different functionalities at different frequencies, opening a door for various new applications. This Master's thesis provides a theoretical analysis for possible alternative ways to realize such a metasurface. Two designs for metasurfaces that demonstrate abilities for wavefront shaping and anomalous refraction are introduced here as well. Numerical simulations for the two proposed designs as well as testing one of them experimentally are also presented. Moreover, a promising approach to design multifunctional cascaded metasurfaces that provide different operations at different frequencies is proposed and numerically tested.

Keywords: metasurface, multifunctional, reflectionless, transmitarray

Preface

Otaniemi, 16.2.2016

Amr Elsakka

Contents

Abstract ii

Preface iii

Contents iv

Symbols and Abbreviations v

1 Introduction 1
- 1.1 Motivation . . . 1
- 1.2 Conventional Structures for Wave Control . . . 2
- 1.3 Metamaterials and Huygens' Metasurfaces . . . 4
- 1.4 Thesis Overview . . . 7

2 Controlling the Phase and Amplitude of Transmission with Single-Wire Huygens' Elements 7
- 2.1 Arrays with Single-Wire Bianisotropic Omega Elements . . . 10
- 2.2 Arrays with Single-Wire Bianisotropic Chiral Elements . . . 10
- 2.3 Non-Bianisotropic Arrays with Single-Wire Elements . . . 12

3 Synthesis of Broadband Reflectionless Transmitarrays 15
- 3.1 Manipulating the Direction of Wave Propagation . . . 17
- 3.2 Wavefront Shaping . . . 18
  - 3.2.1 Simulations . . . 18
  - 3.2.2 Experiment . . . 19

4 Multifunctional Cascaded Metasurfaces 23

5 Conclusions 28

A Appendix 1. Parameters of 45° Refract Array 32

B Appendix 2. Parameters of Metalens 33

C Appendix 3. Parameters of the Multifunctional Structure 35

Symbols and Abbreviations

Symbols

$\mathbf{B}$	Magnetic flux density
$\mathbf{D}$	Electric flux density
$\mathbf{E}$	Electric field vector
$\mathbf{E}_{\mathrm{inc}}$	Incident electric field vector
$\mathbf{E}_{\mathrm{ref}}$	Reflected electric field vector
$\mathbf{E}_{\mathrm{t}}$	Transmitted electric field vector
E_{inc}	Incident electric field amplitude
f	Frequency
F	Focal length
$\mathbf{H}$	Magnetic field vector
$\mathbf{H}_{\mathrm{inc}}$	Incident magnetic field vector
$\mathbf{H}_{\mathrm{ref}}$	Reflected magnetic field vector
$\mathbf{H}_{\mathrm{t}}$	Transmitted electric field vector
H_{inc}	Incident magnetic field amplitude
$\mathbf{J}_{\mathrm{e}}$	Electric current density
$\mathbf{J}_{\mathrm{m}}$	Magnetic current density
$\mathbf{J}_{\mathrm{se}}$	Surface electric current density
$\mathbf{J}_{\mathrm{sm}}$	Surface magnetic current density
$\mathbf{k}_{\mathrm{inc}}$	Wave vector of an incident wave
$\mathbf{k}_{\mathrm{ref}}$	Wave vector of a reflected wave
k_0	Wavenumber of free space
l	Length of metal wire
$\mathbf{m}$	Magnetic dipole moment vector
$\mathbf{n}$	Normal unit vector
$\mathbf{p}$	Electric dipole moment vector
r_0	Wire radius
S	Area of the unit cell
ε_0	Permittivity of free space
ε	Relative permittivity
$\overline{\overline{\widehat{\alpha}}}_{\mathrm{ee}}$	Effective electric polarizability dyadic
$\overline{\overline{\widehat{\alpha}}}_{\mathrm{em}}$	Effective electro-magnetic polarizability dyadic
$\overline{\overline{\widehat{\alpha}}}_{\mathrm{me}}$	Effective magneto-electric polarizability dyadic
$\overline{\overline{\widehat{\alpha}}}_{\mathrm{mm}}$	Effective magnetic polarizability dyadic
$\overline{\overline{\alpha}}_{\mathrm{ee}}$	Individual electric polarizability dyadic
$\overline{\overline{\alpha}}_{\mathrm{em}}$	Individual electro-magnetic polarizability dyadic
$\overline{\overline{\alpha}}_{\mathrm{me}}$	Individual magneto-electric polarizability dyadic
$\overline{\overline{\alpha}}_{\mathrm{mm}}$	Individual magnetic polarizability dyadic
β_{e}	Electric-field interaction constant
β_{m}	Magnetic-field interaction constant
η	Wave impedance

η_0	Wave impedance of free space
ρ_{e}	Electric charge density
ρ_{m}	Magnetic charge density
ρ_{se}	Surface electric charge density
ρ_{sm}	Surface magnetic charge density
κ	Chirality parameter
λ	Wavelength
μ_0	Permeability of free space
μ	Relative permeability
ϕ	Phase
ω	Angular frequency
Ω	Omega-coupling coefficient

Abbreviations and Acronyms

cm	Centimetre
GHz	GigaHertz
HFSS	High Frequency Structure Simulator
mm	Millimetre
PEC	Perfect Electric Conductor
PMC	Perfect Magnetic Conductor
RF	Radio Frequency
SRR	Split Ring Resonator
TEM	Transverse Electromagnetic

1 Introduction

1.1 Motivation

Manipulations of electromagnetic waves in transmission through various structures has been of fundamental importance in a great number of applications. Through interaction of waves with matter it is possible to control the wave intensity, polarization and propagation direction. Almost all known structures for wave manipulation perform a particular functionality in the frequency range they operate, while being not transparent and casting a "shadow" (or producing some disturbance) at other frequencies. Figure 1a illustrates such functionality by the example of Newton's prism. That prism cannot refract the light of one color without disturbing the paths of light of other colors. On the other hand, designing structures that manipulate waves only of specific frequencies, while not interacting with radiation of other frequencies (Fig. 1b illustrates such a scenario), would enable new exciting opportunities. In particular, such devices performing different functionalities at different frequencies could be cascaded and even combined in one *single* structure (if its constitutional elements are of several different types) [see Fig. 1c].

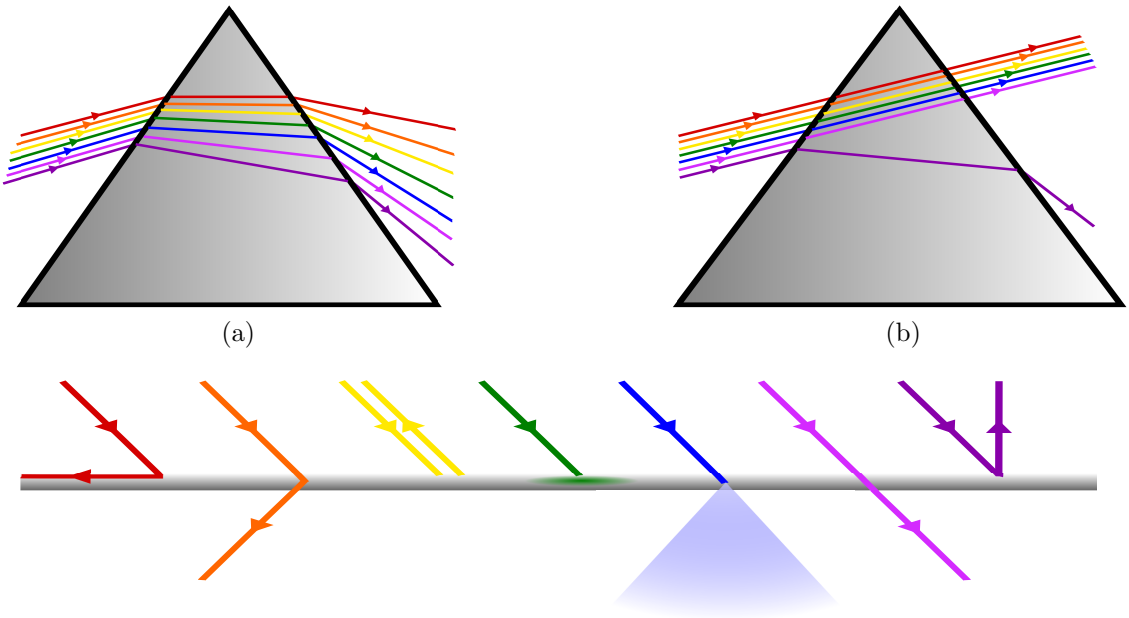

(a) (b) (c)

Figure 1: (a) Light propagation through Newton's prism. The prism refracts the light of all frequencies. (b) Light propagation through a prism that refracts only light of violet color and does not interact with light of other frequencies. (c) Multifunctional multifrequency composite. Incident light of different colors receives different predetermined response from the composite.

Synthesizing such multifunctional devices with compact size and light weight is of great interest to various applications, for example, satellite and radar systems. To

the best of our knowledge, only frequency-selective reflection [1, 2] and absorption [3] in out-of-band transparent sheets were achieved before, therefore, to complete the full set of functionalities for wave control, it is necessary to design a frequency-selective transmitarray, i.e. a structure that tailors transmitted fields of incident waves of desired frequencies and passes through the others. Such metasurfaces can be integrated into a cascade of different devices that all operate independently in a narrow band and are transparent outside of the operating band, performing multifunctional multifrequency operations (see Fig. 1c).

1.2 Conventional Structures for Wave Control

Conventionally, light has been manipulated in transmission using lenses and prisms, which then have evolved into numerous appliances operating at frequencies ranging from radio waves to ultraviolet. The evolution for such devices aimed at reducing size, providing higher efficiency and flexibility, without taking into account the transparency outside of the operating frequency band. For example, the need for decreasing the bulky size of the conventional lens that deals with light, lead to the invention of Fresnel lens. Fresnel lens provides a compact size, large aperture, and short focal length trading imaging quality to compact size (see Fig. 2).

(a) (b)

Figure 2: Examples of conventional lenses (a) Side view of a conventional bulky lens. (b) Side view of a Fresnel lens.

More recently, by utilizing dielectric lenses, electromagnetic waves manipulation capabilities were extended to include radio and microwave frequencies. Dielectric lenses depend on the concept of manipulating the dielectric constant to provide focusing or refraction. Luneburg lens is a well known example of dielectric lenses, it has a spherical shape with a gradual change of the relative permittivity from 2 at the center to 1 at the surface (see Fig. 3a). Various ideas were introduced based on the same concept aiming at compact size and higher efficiency, like what was provided in [4]. That flat structure provided high-directivity, low side-lobe levels, and steerable

capabilities, with similar properties to the original spherical lens (see Fig. 3b). But all those solutions operate in a broad frequency band which will eventually disturb waves at other frequencies and limit the integration capabilities. More about Fresnel and dielectric lenses can be found in [5].

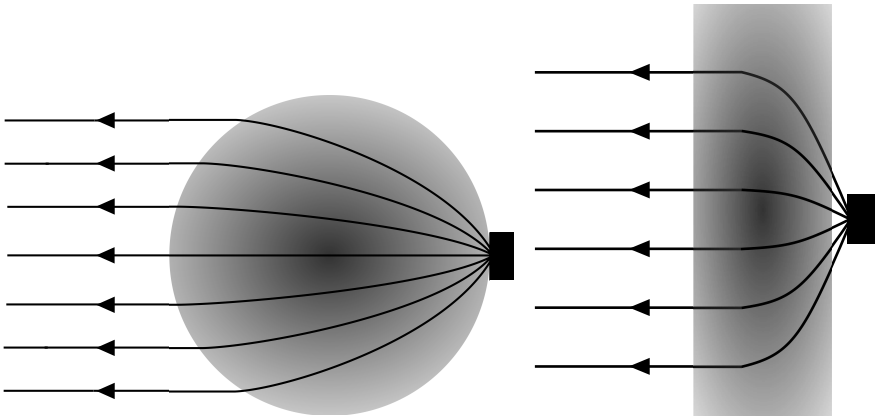

(a) (b)

Figure 3: Examples of conventional lenses, the gradient shows the gradual decrease of the permittivity from the center to the surface. (a) Luneburg lens. (b) Flat Luneburg lens.

Another way to manipulate electromagnetic waves is using antennas. Traditional aperture antennas such as reflectors and lenses are low cost, easy to fabricate, and provide high gain. However, beam steering is only available using mechanical scanning, and beam shaping can only be achieved if more sophisticated feeding systems are used. Antenna arrays are able to overcome the drawbacks of aperture antennas by utilizing electronic circuits to control each element excitation which provides beam steering in real time. The main drawbacks of antenna arrays are the complex and relatively large hardware size, as each antenna element should be connected to a transceiver module which makes the implementation cost high, adding to that the presence of transmission lines for feeding which become very lossy at millimeter wave frequencies [6, 7], etc.

Another candidate could be transmitarray antennas (also called array lenses) invented several decades ago [8, 9]. They significantly extended the opportunities for wave control, enabling wavefront shaping and beam scanning at a single frequency. But again, conventional transmitarray antennas incorporate a ground plane with the receiving and transmitting antenna arrays on its sides connected by matched cables or by other two-port networks. Therefore, transmitarray antennas cannot pass through the incident radiation of frequencies beyond their bands, casting a shadow. Figure 4 shows two examples of antenna transmitarrays.

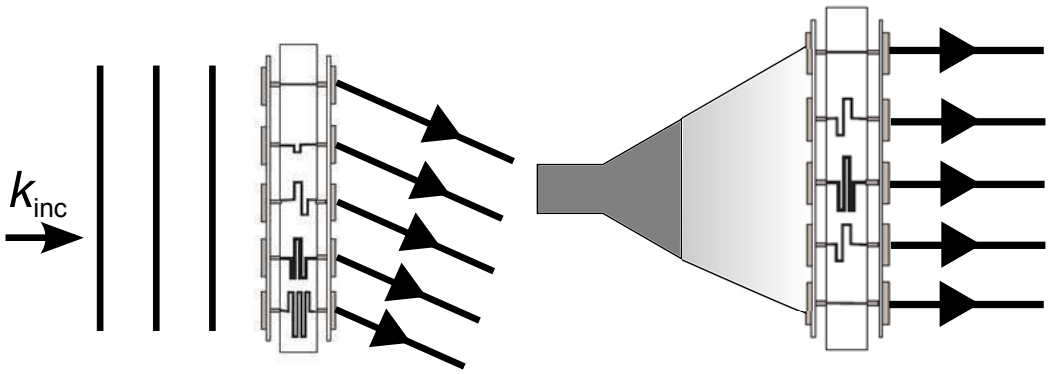

(a) (b)

Figure 4: Examples of antenna transmitarrays. (a) Refract array. (b) Lens.

To summarize, conventional structures provided the required functions efficiently. However, they either operate in a broadband, or in a narrow band but cast a shadow out of their operating band. To be able to integrate several structures into a single composite that will provide different functions at different frequencies, every structure should be operating at a narrow band and be transparent out of its operating band. In the following section metamaterials will be discussed as a potential solution for building such a multifunctional device.

1.3 Metamaterials and Huygens' Metasurfaces

Metamaterials are artificially engineered materials that are composed of elements whose dimensions are reasonably small compared to the operational wavelength. These elements, often called *meta-atoms*, are designed with special size, geometry, and arrangement in order to manipulate electromagnetic waves. The small size of meta-atoms makes the material appear to the incident wave as a homogeneous medium while the artificially designed meta-atoms can be tuned to change the relative permittivity and permeability of the metamaterial to manipulate electromagnetic waves. Metamaterials gained much attention when artificial negative index material (backward-wave material) was introduced in 2000-2001. By interaction of incident electromagnetic waves with such metamaterial, the waves would be negatively refracted and their phase and group velocities would be in opposite directions, as a result of the material negative permittivity and permeability (see Fig. 5).

Figure 5: Illustration for positive and negative refraction

However, negative index material (backward-wave material) was anticipated in theory more than a century ago. It remained theoretical and was not realized for a long time since no one believed that negative index material can exist. Then in 2000 the first realization for that material was introduced. The proposed structure was a volumetric anisotropic structure composed of particles shaped as wires that are electrically polarizable and split ring resonators (SRR) that are magnetically polarizable (see Fig. 6).

Figure 6: Volumetric metamaterial consists of a SSR and a wire element for each unit cell [10]

Various studies were held for bianisotropic materials [11] that are simultaneously electrically and magnetically anisotropic as well as they are magnetoelectrically coupled. A reciprocal bianisotropic medium can be described by the permittivity ϵ, permeability μ, and the field coupling coefficients, such as the chirality parameter

κ, and the omega-coupling coefficient Ω. Omega and chiral coupling coefficients introduce very interesting phenomena. In isotropic chiral materials two circularly polarized waves can propagate in any direction having two different propagation constants, in addition to the independence of the wave impedance on the chiral coupling factor κ. Chiral materials allow synthesis of negative index materials. While in uniaxial omega materials only linearly polarized waves are allowed in either directions and the wave impedance is dependent on the omega coupling factor and the propagation direction. That can allow synthesis of a material slab that acts as PEC from one side and PMC from the other [11].

The main drawbacks of 3D metamaterials are that they are lossy and hard to fabricate and integrate in other devices. Thin-layer 2D metasurfaces overcome those drawbacks. Metasurfaces possess smaller losses, and are of compact size, and simple to manufacture which make them of great interest to many applications. Metasurfaces can be built based on the Huygens principle. The Huygens principle states that every point on the wavefront can be represented as a secondary source of a spherical wave which interferes with the waves outgoing from the sources next to it producing the original wavefront. These secondary sources can be represented physically by electrically small radiating elements that exhibit electric and magnetic dipoles perpendicular to each other. Huygens metasurfaces utilize this concept by being built of electically small elements that are electrically and magnetically polarizable so that the dipole moments induced in each element form Huygens' pairs. Therefore, each element does not scatter in the backward direction, while it radiates waves with the prescribed phase and amplitude in the forward direction. The forward scattered waves from the elements form the transmitted wave. By tuning the properties of the metasurface dipoles, manipulation of electromagnetic wavefront in transmission can be achieved with minimal reflections. It is necessary to design the elements of the metasurface so that they can provide full phase control (from 0 to 2π) for the forward scattered waves, that will lead to full manipulation capability of the transmitted waves.

Recently, there have been considerable interest and progress in manipulation of electromagnetic waves using metasurfaces [12–23]. It should be noted that in all known transmitarray metasurfaces the structural elements constitute reflectionless Huygens' sources only inside a narrow frequency band. Beyond this band reflections appear because of prevailing excitation of either electric or magnetic dipole. This is due to the fact that these elements have different frequency dispersions of the electric and magnetic dipole modes (see [3]).

In order to design a structure that fully manipulates transmitted waves and is invisible for incident radiation outside of the operational band (see Fig. 1b), its elements should provide full phase control, and they should be designed in such a way that the electric and magnetic dipole moments, induced in them, are balanced (have equal amplitudes) at all practically relevant frequencies. This implies that both dipole responses should be created by excitation of the same resonant mode (the dipole moments are formed by the same current distribution in the element). Such regime is possible only if each element consists of a *single* conductive wire [3]. These wire elements inevitably possess bianisotropic properties [11]. In earlier work, such

scenario was realized only for absorbers [3], but not for transmitarrays.

1.4 Thesis Overview

This thesis presents synthesis of a uniaxial (isotropic in its plane) low-loss reciprocal metasurface that transforms the wavefront of incident waves in a desired manner (in transmission) at the desired frequency, while remaining transparent in a wide frequency band. It also provides a theoretical analysis for all possible scenarios of realization of such a metasurface and determination of the unique requirements for the electromagnetic response of its elements. Here also design and measurement of two synthesized metasurfaces that demonstrate abilities for wavefront shaping and anomalous refraction are provided. Moreover, a promising approach to design multifunctional cascaded metasurfaces that provide different operations at different frequencies (see Fig. 1c) is offered. This approach, generally, can be extended to volumetric metamaterials. Finally, that approach is verified by providing a design solution for integrated metasurfaces that provides three basic functions such as full control over reflection, absorption and transmission properties. That cascaded composite will be built using previously designed reflectionless metasurfaces and will be numerically simulated.

2 Controlling the Phase and Amplitude of Transmission with Single-Wire Huygens' Elements

Manipulation of waves transmitted through a thin metasurface can be accomplished due to specifically designed phase gradients over the metasurface plane [12, 13, 24]. The phase gradient can be achieved by precise adjustment of the phases of transmitted waves from each metasurface inclusion. To adjust the phases for each inclusion, the locally uniform homogenization approach is used, i.e. the inclusion is tuned assuming that it is located in an array with a uniform phase distribution. An array of such individually adjusted inclusions possesses nearly the required non-uniform phase distribution. Therefore, it is important to design individual inclusions so that uniform arrays, formed by them, transmit incident waves, conserving their amplitude but changing their phase by a specific value ϕ (different for each inclusion) that belongs to the interval from 0 to 2π. Next, all possible scenarios of designing metasurface elements that satisfy these conditions will be examined.

Let us consider a reciprocal metasurface as a two-dimensional periodic array of sub-wavelength bianisotropic inclusions polarizable electrically and magnetically. The ability of an individual inclusion to get polarized in external electric and magnetic fields is described, respectively, by the polarizability tensors $\overline{\overline{\alpha}}_{\mathrm{ee}}$ and $\overline{\overline{\alpha}}_{\mathrm{mm}}$. The bianisotropy implies that the electric (magnetic) field of the incident wave can also produce magnetic (electric) polarization in the inclusions. This effect is often called magnetoelectric coupling and can be characterized by the magnetoelectric polarizability dyadic $\overline{\overline{\alpha}}_{\mathrm{me}}(\overline{\overline{\alpha}}_{\mathrm{em}})$. The linear relations between the local fields (at the location of the inclusion) and the induced dipole moments are as follows [11]:

$$\begin{bmatrix}\mathbf{p}\\ \mathbf{m}\end{bmatrix} = \begin{bmatrix}\overline{\overline{\alpha}}_{\mathrm{ee}} & \overline{\overline{\alpha}}_{\mathrm{em}}\\ \overline{\overline{\alpha}}_{\mathrm{me}} & \overline{\overline{\alpha}}_{\mathrm{mm}}\end{bmatrix} \cdot \begin{bmatrix}\mathbf{E}_{\mathrm{loc}}\\ \mathbf{H}_{\mathrm{loc}}\end{bmatrix}, \tag{1}$$

where $\mathbf{E}_{\mathrm{loc}}$ and $\mathbf{H}_{\mathrm{loc}}$ are the sums of the incident field and the interaction fields caused by the induced dipole moments in all particles:

$$\begin{aligned}\mathbf{E}_{\mathrm{loc}} &= \mathbf{E}_{\mathrm{inc}} + \overline{\overline{\beta}}_{\mathrm{e}} \cdot \mathbf{p},\\ \mathbf{H}_{\mathrm{loc}} &= \mathbf{H}_{\mathrm{inc}} + \overline{\overline{\beta}}_{\mathrm{m}} \cdot \mathbf{m}.\end{aligned} \tag{2}$$

Here $\overline{\overline{\beta}}_{\mathrm{e}}$ and $\overline{\overline{\beta}}_{\mathrm{m}}$ are the interaction factors that describe the effect of the whole array on the individual inclusion. For the metasurface synthesis it is convenient to express the induced dipole moments in terms of the incident fields. By substituting (2) in (1) and solving the system of linear equations for the dipole moments, we find the following relations:

$$\begin{bmatrix}\mathbf{p}\\ \mathbf{m}\end{bmatrix} = \begin{bmatrix}\overline{\overline{\hat{\alpha}}}_{\mathrm{ee}} & \overline{\overline{\hat{\alpha}}}_{\mathrm{em}}\\ \overline{\overline{\hat{\alpha}}}_{\mathrm{me}} & \overline{\overline{\hat{\alpha}}}_{\mathrm{mm}}\end{bmatrix} \cdot \begin{bmatrix}\mathbf{E}_{\mathrm{inc}}\\ \mathbf{H}_{\mathrm{inc}}\end{bmatrix}, \tag{3}$$

where $\overline{\overline{\hat{\alpha}}}_{\mathrm{ee}}$, $\overline{\overline{\hat{\alpha}}}_{\mathrm{mm}}$, and $\overline{\overline{\hat{\alpha}}}_{\mathrm{em}}$, are the effective polarizabilities which are functions of the interaction factors and polarizabilities of the individual inclusions [25].

For reciprocal structures the Onsager-Casimir principle which represents the time reversal symmetry of the Maxwell equations applies, leading to $\overline{\overline{\hat{\alpha}}}_{\mathrm{ee}} = (\overline{\overline{\hat{\alpha}}}_{\mathrm{ee}})^T$, $\overline{\overline{\hat{\alpha}}}_{\mathrm{mm}} = (\overline{\overline{\hat{\alpha}}}_{\mathrm{mm}})^T$, and $\overline{\overline{\hat{\alpha}}}_{\mathrm{me}} = -(\overline{\overline{\hat{\alpha}}}_{\mathrm{em}})^T$ [11], where T denotes the transpose operation. Considering the uniaxial symmetry of the metasurface, it is convenient to represent the polarizability dyadics in the following form:

$$\begin{aligned}\overline{\overline{\hat{\alpha}}}_{\mathrm{ee}} &= \hat{\alpha}^{\mathrm{co}}_{\mathrm{ee}}\overline{\overline{I}}_{\mathrm{t}} + \hat{\alpha}^{\mathrm{cr}}_{\mathrm{ee}}\overline{\overline{J}}_{\mathrm{t}}, \qquad \overline{\overline{\hat{\alpha}}}_{\mathrm{mm}} = \hat{\alpha}^{\mathrm{co}}_{\mathrm{mm}}\overline{\overline{I}}_{\mathrm{t}} + \hat{\alpha}^{\mathrm{cr}}_{\mathrm{mm}}\overline{\overline{J}}_{\mathrm{t}},\\ \overline{\overline{\hat{\alpha}}}_{\mathrm{em}} &= \hat{\alpha}^{\mathrm{co}}_{\mathrm{em}}\overline{\overline{I}}_{\mathrm{t}} + \hat{\alpha}^{\mathrm{cr}}_{\mathrm{em}}\overline{\overline{J}}_{\mathrm{t}}, \qquad \overline{\overline{\hat{\alpha}}}_{\mathrm{me}} = \hat{\alpha}^{\mathrm{co}}_{\mathrm{me}}\overline{\overline{I}}_{\mathrm{t}} + \hat{\alpha}^{\mathrm{cr}}_{\mathrm{me}}\overline{\overline{J}}_{\mathrm{t}},\end{aligned} \tag{4}$$

where $\overline{\overline{I}}_{\mathrm{t}}$ and $\overline{\overline{J}}_{\mathrm{t}}$ are the transverse unit and vector-product dyadics, respectively, and the indices co and cr refer to the symmetric and antisymmetric parts of the corresponding dyadics. The transmitted and reflected fields from the metasurface read [25]:

$$\mathbf{E}_{\mathrm{r}} = -\frac{j\omega}{2S}\left[[\eta_0\hat{\alpha}^{\mathrm{co}}_{\mathrm{ee}}+\hat{\alpha}^{\mathrm{cr}}_{\mathrm{em}}+\hat{\alpha}^{\mathrm{cr}}_{\mathrm{me}}-\frac{1}{\eta_0}\hat{\alpha}^{\mathrm{co}}_{\mathrm{mm}}]\overline{\overline{I}}_{\mathrm{t}}+[\eta_0\hat{\alpha}^{\mathrm{cr}}_{\mathrm{ee}}-\hat{\alpha}^{\mathrm{co}}_{\mathrm{em}}-\hat{\alpha}^{\mathrm{co}}_{\mathrm{me}}-\frac{1}{\eta_0}\hat{\alpha}^{\mathrm{cr}}_{\mathrm{mm}}]\overline{\overline{J}}_{\mathrm{t}}\right]\cdot\mathbf{E}_{\mathrm{inc}}, \tag{5}$$

$$\mathbf{E}_{\mathrm{t}} = \left[\left[1-\frac{j\omega}{2S}(\eta_0\hat{\alpha}^{\mathrm{co}}_{\mathrm{ee}}+\hat{\alpha}^{\mathrm{cr}}_{\mathrm{em}}-\hat{\alpha}^{\mathrm{cr}}_{\mathrm{me}}+\frac{1}{\eta_0}\hat{\alpha}^{\mathrm{co}}_{\mathrm{mm}})\right]\overline{\overline{I}}_{\mathrm{t}}-\frac{j\omega}{2S}\left[\eta_0\hat{\alpha}^{\mathrm{cr}}_{\mathrm{ee}}-\hat{\alpha}^{\mathrm{co}}_{\mathrm{em}}+\hat{\alpha}^{\mathrm{co}}_{\mathrm{me}}+\frac{1}{\eta_0}\hat{\alpha}^{\mathrm{cr}}_{\mathrm{mm}}\right]\overline{\overline{J}}_{\mathrm{t}}\right]\cdot\mathbf{E}_{\mathrm{inc}}, \tag{6}$$

where ω is the angular frequency, S is the area of the array unit cell, and η_0 is the free-space wave impedance.

In this work the study is limited by considering the case of passive reciprocal layers since the non-reciprocal case is usually not practical due to realization complexity, and active case will require a circuitry to provide power to the inclusions. Taking into account the reciprocity of the metasurface, equations (4) can be rewritten as

$$\begin{aligned} \overline{\overline{\widehat{\alpha}}}_{\mathrm{ee}} &= \widehat{\alpha}_{\mathrm{ee}}^{\mathrm{co}}\overline{\overline{I}}_{\mathrm{t}}, & \overline{\overline{\widehat{\alpha}}}_{\mathrm{mm}} &= \widehat{\alpha}_{\mathrm{mm}}^{\mathrm{co}}\overline{\overline{I}}_{\mathrm{t}}, \\ \overline{\overline{\widehat{\alpha}}}_{\mathrm{em}} &= \widehat{\alpha}_{\mathrm{em}}^{\mathrm{co}}\overline{\overline{I}}_{\mathrm{t}} + \widehat{\alpha}_{\mathrm{em}}^{\mathrm{cr}}\overline{\overline{J}}_{\mathrm{t}}, & \overline{\overline{\widehat{\alpha}}}_{\mathrm{me}} &= -\widehat{\alpha}_{\mathrm{em}}^{\mathrm{co}}\overline{\overline{I}}_{\mathrm{t}} + \widehat{\alpha}_{\mathrm{em}}^{\mathrm{cr}}\overline{\overline{J}}_{\mathrm{t}}. \end{aligned} \tag{7}$$

Assuming that the incident wave impinges on the uniaxial metasurface normally to its surface along the $-z$-axis, the electric fields of the reflected and transmitted plane waves from the metasurface are given by [25]

$$\mathbf{E}_{\mathrm{r}} = -\frac{j\omega}{2S}\left[\eta_0\widehat{\alpha}_{\mathrm{ee}}^{\mathrm{co}} + 2\widehat{\alpha}_{\mathrm{em}}^{\mathrm{cr}} - \frac{1}{\eta_0}\widehat{\alpha}_{\mathrm{mm}}^{\mathrm{co}}\right]\cdot\mathbf{E}_{\mathrm{inc}}, \tag{8}$$

$$\mathbf{E}_{\mathrm{t}} = \left[\left(1 - \frac{j\omega}{2S}\left[\eta_0\widehat{\alpha}_{\mathrm{ee}}^{\mathrm{co}} + \frac{1}{\eta_0}\widehat{\alpha}_{\mathrm{mm}}^{\mathrm{co}}\right]\right)\overline{\overline{I}}_{\mathrm{t}} + \frac{j\omega}{S}\widehat{\alpha}_{\mathrm{em}}^{\mathrm{co}}\overline{\overline{J}}_{\mathrm{t}}\right]\cdot\mathbf{E}_{\mathrm{inc}}. \tag{9}$$

As discussed in the introduction section 1.4, to realize broadband reflectionless regime, the metasurface elements must be bianisotropic single-wire inclusions (see examples in Fig. 7).

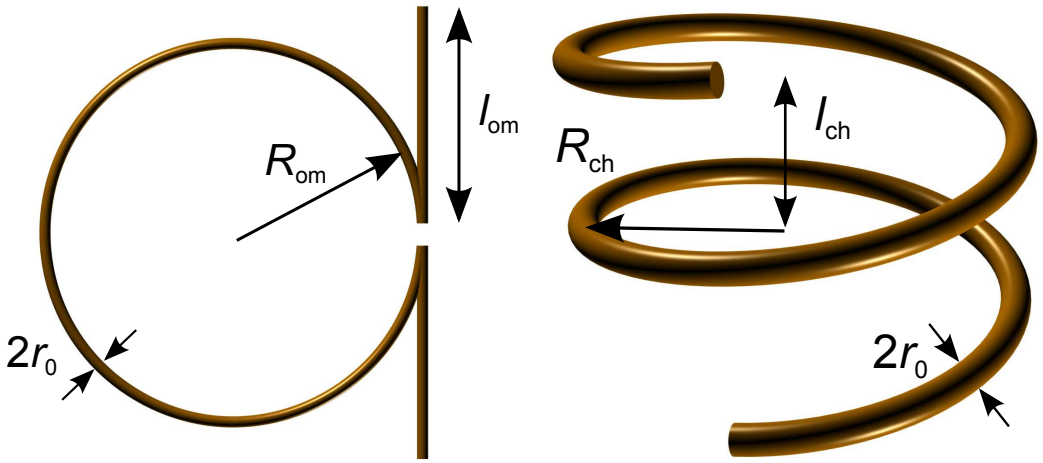

Figure 7: Examples of bianisotropic single-wire inclusions. (a) Omega inclusion. (b) Chiral inclusion.

Bianisotropy is usually classified into two classes as previously mentioned: chiral class with symmetric electromagnetic dyadic ($\widehat{\alpha}_{\mathrm{em}}^{\mathrm{cr}} = 0$) and omega class, when the dyadic is antisymmetric ($\widehat{\alpha}_{\mathrm{em}}^{\mathrm{co}} = 0$) [11, 26]. Based on the same classification, for the sake of clarity, we consider these two cases separately.

2.1 Arrays with Single-Wire Bianisotropic Omega Elements

For a uniform array of single-wire omega inclusions (see Fig. 7a) the following relation between the effective polarizabilities of each inclusion holds [11, 26]:

$$\widehat{\alpha}_{\rm ee}^{\rm co}\widehat{\alpha}_{\rm mm}^{\rm co} = -\widehat{\alpha}_{\rm em}^{\rm cr}\widehat{\alpha}_{\rm me}^{\rm cr} = -(\widehat{\alpha}_{\rm em}^{\rm cr})^2. \tag{10}$$

Substituting $\widehat{\alpha}_{\rm em}^{\rm cr}$ from (10) in (8), we find the fields of reflected waves from the omega metasurface:

$$\mathbf{E}_{\rm r} = -\frac{j\omega}{2S}\left[\eta_0\widehat{\alpha}_{\rm ee}^{\rm co} + 2\sqrt{-\widehat{\alpha}_{\rm ee}^{\rm co}\widehat{\alpha}_{\rm mm}^{\rm co}} - \frac{1}{\eta_0}\widehat{\alpha}_{\rm mm}^{\rm co}\right]\cdot\mathbf{E}_{\rm inc}. \tag{11}$$

Thus, the condition of zero reflection essential for our transmitarray ($\mathbf{E}_{\rm r} = 0$) implies a limitation on the effective polarizabilitities:

$$\widehat{\alpha}_{\rm ee}^{\rm co} = -\frac{1}{\eta_0^2}\widehat{\alpha}_{\rm mm}^{\rm co}. \tag{12}$$

This limitation for effective polarizabilities (which take into account interactions between the inclusions) leads to the corresponding limitation for the individual polarizabilities (modelling the properties of an individual particle in free space) [26]: $\alpha_{\rm ee}^{\rm co} = (-1/\eta_0^2)\,\alpha_{\rm mm}^{\rm co}$. This condition, obviously, cannot be satisfied with passive inclusions. Indeed, the opposite signs of the electric and magnetic polarizabilities imply that their imaginary parts have the opposite signs. This scenario corresponds to the case of a passive-active pair of dipole moments. Furthermore, one can see from (9) [assuming $\widehat{\alpha}_{\rm em}^{\rm co} = 0$] and (12) that in this case the phase of the transmitted wave through the metasurface is always equal to that of the incident wave ($\mathbf{E}_{\rm t} = \mathbf{E}_{\rm inc}$). Thus, it is impossible to synthesize a transmitarray with the desired properties using single-wire omega elements.

2.2 Arrays with Single-Wire Bianisotropic Chiral Elements

Likewise, effective polarizabilities of chiral single-wire inclusions (see Fig. 7b) in a uniform array are related to one another as follows [11, 26]:

$$\widehat{\alpha}_{\rm ee}^{\rm co}\widehat{\alpha}_{\rm mm}^{\rm co} = \widehat{\alpha}_{\rm em}^{\rm co}\widehat{\alpha}_{\rm me}^{\rm co} = -(\widehat{\alpha}_{\rm em}^{\rm co})^2. \tag{13}$$

One can see from (8) that in the case of a chiral metasurface ($\widehat{\alpha}_{\rm em}^{\rm cr} = 0$), the condition of zero reflection ($\mathbf{E}_{\rm r} = 0$) simply requires the balanced electric and magnetic dipoles $\widehat{\alpha}_{\rm ee}^{\rm co} = (1/\eta_0^2)\,\widehat{\alpha}_{\rm mm}^{\rm co}$ of each metasurface inclusion. Comparing to 12, we see that in this case there is no problem in realizations using only passive inclusions, because the imaginary parts of both these polarizabilities have the same sign for passive particles. Taking this result into account and combining it with relation (13), the transmitted fields through the chiral metasurface (9) can be written as

$$\mathbf{E}_{\rm t} = \left[\left(1 - \frac{j\omega}{S}\eta_0\widehat{\alpha}_{\rm ee}^{\rm co}\right)\overline{\overline{I}}_{\rm t} \pm \frac{\omega}{S}\eta_0\widehat{\alpha}_{\rm ee}^{\rm co}\overline{\overline{J}}_{\rm t}\right]\cdot\mathbf{E}_{\rm inc}, \tag{14}$$

where the upper and lower signs correspond to chiral inclusions with right and left handedness, respectively. From (14) it is seen that, generally, the polarization of the wave transmitted through a chiral transmitarray is different from that of the incident wave. In designs of conventional transmitarrays almost always it is assumed that the polarization of the wave passing through a transmitarray does not change. However, in many applications polarization-plane rotation of transmitted waves (in focusing arrays designed for circularly polarized waves, for example), is acceptable. Thus, it is important to consider also the case when the transmitarray transforms the incident wave polarization, since if there is no requirement for keeping the polarization the same, there is more design freedom in transmitarrays realizations. Therefore, we look for a solution for the transmitted field in the most general form of elliptic polarization:

$$\mathbf{E}_{\mathrm{t}} = (T_{\mathrm{co}}\overline{\overline{I}}_{\mathrm{t}} + T_{\mathrm{cr}}e^{j\Delta\phi}\overline{\overline{J}}_{\mathrm{t}})e^{j\phi}\cdot\mathbf{E}_{\mathrm{inc}}, \tag{15}$$

where $\Delta\phi$ is the phase difference between the two orthogonal components of the elliptically polarized transmitted field, T_{co} and T_{cr} are the semi-major and semi-minor axes of the polarization ellipse (real values), and ϕ is the phase shift between the incident wave (assumed to be linearly polarized) and the elliptically polarized transmitted wave.

Comparing (14) and (15), we find

$$T_{\mathrm{co}} = |1 - \frac{j\omega}{S}\eta_0\widehat{\alpha}_{\mathrm{ee}}^{\mathrm{co}}|, \qquad \phi = \angle(1 - \frac{j\omega}{S}\eta_0\widehat{\alpha}_{\mathrm{ee}}^{\mathrm{co}}), \tag{16}$$

$$T_{\mathrm{cr}} = |\frac{\omega}{S}\eta_0\widehat{\alpha}_{\mathrm{ee}}^{\mathrm{co}}|, \qquad \phi + \Delta\phi = \angle(\pm\frac{\omega}{S}\eta_0\widehat{\alpha}_{\mathrm{ee}}^{\mathrm{co}}), \tag{17}$$

where symbol $\angle$ denotes the phase angle of the exponential representation of a complex number.

From the energy conservation in lossless metasurfaces it follows that $T_{\mathrm{co}}^2 + T_{\mathrm{cr}}^2 = 1$, which connects the real and imaginary parts of the electric polarizability of each unit cell:

$$\Re\{\widehat{\alpha}_{\mathrm{ee}}^{\mathrm{co}}\} = \pm\sqrt{-\Im\{\widehat{\alpha}_{\mathrm{ee}}^{\mathrm{co}}\}\left(\frac{S}{\omega\eta_0} + \Im\{\widehat{\alpha}_{\mathrm{ee}}^{\mathrm{co}}\}\right)}. \tag{18}$$

Using (18), we can rewrite (16) and (17) as

$$T_{\mathrm{co}} = \sqrt{1 + \frac{\omega}{S}\eta_0\Im\{\widehat{\alpha}_{\mathrm{ee}}^{\mathrm{co}}\}}, \qquad T_{\mathrm{cr}} = \sqrt{-\frac{\omega}{S}\eta_0\Im\{\widehat{\alpha}_{\mathrm{ee}}^{\mathrm{co}}\}}, \tag{19}$$

$$\phi = \mp\operatorname{arccot}\sqrt{-\frac{S}{\omega\eta_0\Im\{\widehat{\alpha}_{\mathrm{ee}}^{\mathrm{co}}\}} - 1}, \tag{20}$$

and $\Delta\phi = 0$.

It should be noted that in order to achieve the maximum efficiency, all the elements of the transmitarray must radiate waves of the same polarization, ensuring constructive interference. This implies that the polarization parameters T_{co} and T_{cr} should be equal for all the elements. Therefore, from (19) one can see that the imaginary part of the polarizability $\Im\{\widehat{\alpha}_{\mathrm{ee}}^{\mathrm{co}}\}$ must be the same for all the elements.

Evidently, in this case, from (20) we see that the phases of the transmitted waves from each element ϕ are equal and cannot be adjusted arbitrarily. This fact forbids designing efficient transmitarrays for wavefront control from bianisotropic arrays with single-wire chiral inclusions.

2.3 Non-Bianisotropic Arrays with Single-Wire Elements

In the previous sections it was shown that design of a transmitarray which is "invisible" beyond its operational band requires the use of bianisotropic single-wire inclusions. On the other hand, it was demonstrated that bianisotropic arrays of single-wire inclusions do not provide full phase control from 0 to 2π. The only solution to overcome these two contradictory statements is designing a transmitarray whose each unit cell consists of bianisotropic inclusions, being in overall not bianisotropic. This situation is possible if the bianisotropic effects of the inclusions in a single unit cell are mutually compensated. To realize it, one can compose a unit cell of inclusions with the opposite (by sign) bianisotropy parameters. Therefore, there can be two different but equivalent scenarios: a unit cell consists of chiral inclusions with left and right handedness [3,27] and a unit cell consists of oppositely oriented omega inclusions [28]. In both these cases the bianisotropic effects are completely compensated and the unit cell behaves as a pair of orthogonal electric and magnetic dipoles. However, in contrast to the well known unit cells consisting of a split ring resonator and a continuous wire [10,29], this anisotropic unit cell made of bianisotropic elements is reflectionless and "invisible" over a very broad frequency range.

The field expressions (8) and (9) for the array of single-wire inclusions with compensated bianisotropy we rewrite as

$$\mathbf{E}_{\mathrm{r}} = -\frac{j\omega}{2S}\left[\eta_0\widehat{\alpha}_{\mathrm{ee}}^{\mathrm{co}} - \frac{1}{\eta_0}\widehat{\alpha}_{\mathrm{mm}}^{\mathrm{co}}\right]\cdot\mathbf{E}_{\mathrm{inc}}, \tag{21}$$

$$\mathbf{E}_{\mathrm{t}} = \left[1 - \frac{j\omega}{2S}\Big(\eta_0\widehat{\alpha}_{\mathrm{ee}}^{\mathrm{co}} + \frac{1}{\eta_0}\widehat{\alpha}_{\mathrm{mm}}^{\mathrm{co}}\Big)\right]\cdot\mathbf{E}_{\mathrm{inc}}, \tag{22}$$

where reflection from the metasurface is suppressed, only if the dipole moments of the unit cells are balanced $\widehat{\alpha}_{\mathrm{ee}}^{\mathrm{co}} = (1/\eta_0^2)\,\widehat{\alpha}_{\mathrm{mm}}^{\mathrm{co}}$. From [25] the relation that connects the indvidual and collective polarizability reads:

$$\frac{1}{\eta_0\alpha_{\mathrm{ee}}} = \frac{1}{\eta_0\widehat{\alpha}_{\mathrm{ee}}} + \frac{\beta_{\mathrm{e}}}{\eta_0}. \tag{23}$$

From [30] an expression for β_{e} with approximate real part and exact imaginary part reads:

$$\beta_{\mathrm{e}} = \Re\left\{-\frac{jk_0}{4\epsilon_0\mathrm{S}}\Big(1 - \frac{1}{jk_0\rho}\Big)e^{-jk_0\rho}\right\} + \frac{j}{\eta_0}\Big(\frac{k_0^3}{6\pi\epsilon_0} - \frac{k_0}{2\epsilon_0\mathrm{S}}\Big), \tag{24}$$

where $\rho = \dfrac{a}{1.438}$, and a is the array period.

$$\Rightarrow \frac{1}{\eta_0\widehat{\alpha}_{\mathrm{ee}}^{\mathrm{co}}} = \frac{1}{\widehat{\alpha}_{\mathrm{mm}}^{\mathrm{co}}/\eta_0} = \Re\left\{\frac{1}{\eta_0\alpha_{\mathrm{ee}}^{\mathrm{co}}}\right\} - \frac{1}{\eta_0}\Re\left\{\beta_{\mathrm{e}}\right\} + j\Im\left\{\frac{1}{\eta_0\alpha_{\mathrm{ee}}^{\mathrm{co}}}\right\} - \frac{j}{\eta_0}\Big(\frac{k_0^3}{6\pi\epsilon_0} - \frac{k_0}{2\epsilon_0\mathrm{S}}\Big). \tag{25}$$

From [31], the following relation applies for any lossless scatterer:

$$\Im\left\{\frac{1}{\alpha_{\mathrm{ee}}^{\mathrm{co}}}\right\} = \frac{k_0^3}{6\pi\epsilon_0}, \tag{26}$$

$$\Rightarrow \frac{1}{\eta_0\widehat{\alpha}_{\mathrm{ee}}^{\mathrm{co}}} = \frac{1}{\widehat{\alpha}_{\mathrm{mm}}^{\mathrm{co}}/\eta_0} = \Re\left\{\frac{1}{\eta_0\alpha_{\mathrm{ee}}^{\mathrm{co}}}\right\} - \frac{1}{\eta_0}\Re\left\{\beta_{\mathrm{e}}\right\} + j\frac{\omega}{2\mathrm{S}}. \tag{27}$$

Assuming Lorentz dispersion for indvidual polarizabilities, equation (27) can be rewritten as:

$$\frac{1}{\eta_0\widehat{\alpha}_{\mathrm{ee}}} = \frac{1}{\widehat{\alpha}_{\mathrm{mm}}^{\mathrm{co}}/\eta_0} = \frac{\omega_{\mathrm{e}}^2 - \omega^2}{\mathrm{A_e}} + j\frac{\omega}{2\mathrm{S}}. \tag{28}$$

One can find from (22) and (28) the fields transmitted through the metasurface:

$$\mathbf{E}_{\mathrm{t}} = \left[1 - \frac{j\omega}{S}\eta_0\widehat{\alpha}_{\mathrm{ee}}^{\mathrm{co}}\right]\cdot\mathbf{E}_{\mathrm{inc}} = \frac{\mathrm{S}\left(\dfrac{\omega_{\mathrm{e}}^2 - \omega^2}{\mathrm{A_e}}\right) - \mathrm{j}\dfrac{\omega}{2}}{\mathrm{S}\left(\dfrac{\omega_{\mathrm{e}}^2 - \omega^2}{\mathrm{A_e}}\right) + \mathrm{j}\dfrac{\omega}{2}} \tag{29}$$

$$\Rightarrow \mathbf{E}_{\mathrm{t}} = e^{-j\phi_{\mathrm{t}}}\cdot\mathbf{E}_{\mathrm{inc}}, \tag{30}$$

where

$$\phi_{\mathrm{t}} = 2\arctan\left(\frac{\omega\eta_0}{2S}\frac{1}{\Re\left\{1/\widehat{\alpha}_{\mathrm{ee}}^{\mathrm{co}}\right\}}\right). \tag{31}$$

It is clear from equation (31) that the magnitude of the transmission coefficient is one, and the phase can range from 0 to 2π, as the arctangent function varies over π, therefore, ϕ_{t} varies over 2π as a result of multiplying the arctangent by 2.

Figure 8a shows the amplitude and phase of the transmitted wave, dictated by (30) and (31), through a uniform anisotropic array of single-wire inclusions. Here we have assumed that the real part of the individual polarizability of the unit cell has Lorentzian dispersion $\Re\left\{1/\widehat{\alpha}_{\mathrm{ee}}^{\mathrm{co}}\right\} = (\omega_{\mathrm{e}}^2 - \omega^2)/\mathrm{A_e}$, where $\mathrm{A_e} = 3000\ \mathrm{m^2\cdot rad^2/(s\cdot Ohm)}$ and $\omega_{\mathrm{e}} = 2.81\times10^{10}$ rad/s have been chosen to correlate with the numerical results described in the next section.

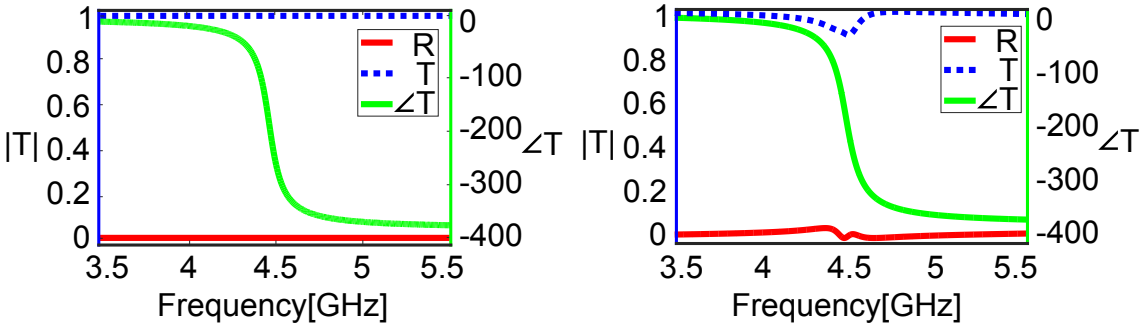

Figure 8: Reflectance R, Transmittance T and phase of transmission $\angle$ from a periodic array of single-wire inclusions. (a) Theoretical model of a lossless anisotropic metasurface. (b) Numerical results for the structure depicted in Fig. 9.

It is seen that the amplitude of the transmitted wave is identically equal to unity at all frequencies, while its phase spans a full 2π range (the arctangent function in (31) varies over π, therefore, $\phi_{\rm t}$ varies over 2π). Similar frequency dispersions were explored in [32]. Since in our transmitarray all the unit cells should operate at the same frequency, the required phase variations can be achieved by adjusting the polarizability $\alpha_{\rm ee}^{\rm co}$ according to (31). The simplest way to control the polarizability strength of the unit cell is to scale proportionally all the sizes of its inclusions. As is seen from Fig. 8a, at the resonance (4.47 GHz), the phase of transmission is $-\pi$. If we fix this frequency as the operational one, downscaling all the dimensions of the unit-cell inclusions will result in phase increase (from $-\pi$ towards 0) of the transmitted wave at the operational frequency. Upscaling the inclusions, vice versa, will lead to the phase decrease (from $-\pi$ towards -2π).

It is simple to prove that a metasurface possessing only electric dipole response ($\widehat{\alpha}_{\rm mm}^{\rm co}=0$) cannot provide full phase variation of transmission. Indeed, in this case reflections from the metasurface inevitably appear $\mathbf{E}_{\rm r}\neq 0$ and the phase of the transmitted wave

$$\phi_{\rm t}=\arctan\left(\frac{\omega\eta_0}{2S}\frac{1}{\Re\left\{1/\widehat{\alpha}_{\rm ee}^{\rm co}\right\}}\right) \tag{32}$$

spans only the π range. Therefore, metasurfaces possessing solely electric dipole response (commonly called in literature single-layer frequency selective surfaces) cannot have 100% efficiency [12, 13, 24].

In summary, this analysis shows that broadband reflectionless uniaxial transmitarrays can be realized only with bianisotropic single-wire inclusions whose electromagnetic coupling is compensated on the level of the unit cell. In this case, the polarization of the transmitted wave is the same as that of the incident one. Importantly, polarization plane rotation is impossible in such transmitarrays.

3 Synthesis of Broadband Reflectionless Transmitarrays

Based on the preceding theoretical analysis, transmitarrays from chiral helical inclusions (see Fig. 7b) are synthesized, where the chirality is compensated on the level of the unit cell. Alternatively, one could use inclusions with omega electromagnetic coupling. Without loss of generality, in this thesis we design transmitarrays operating in microwaves on account of peculiarities of the inclusions fabrication. Arrays of helical inclusions operating at infrared frequencies can be manufactured based on fabrication technologies reported in [33, 34]. First, it is important to design the unit-cell topology with suppressed chirality. To ensure uniaxial symmetry, the unit cell should contain helices oriented in two orthogonal directions in the metasurface plane. The arrangement of helices proposed in [3,35] is utilized and shown in Fig. 9a.

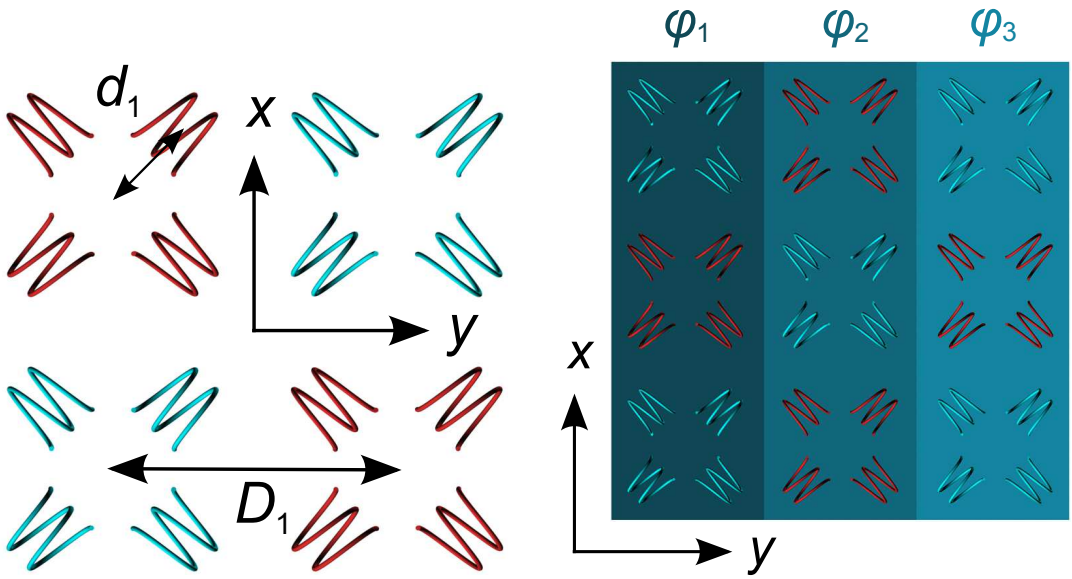

(a) (b)

Figure 9: (a) Arrangement of the inclusions in the unit cell. Left- and right-handed inclusions are shown in red and blue, respectively. (b) Phase variations over the transmitarray. Different background colors denote blocks of helices with different phases ϕ_1, ϕ_2 and ϕ_3.

The unit cell includes two blocks of left-handed and two blocks of right-handed helices. The sub-wavelength size of the inclusions ensures that the unit cell size $2D_1$ is smaller than the operational wavelength. Therefore, arrays of such unit cells can be modeled as sheets of homogeneous surface electric and magnetic currents, and the reflected and transmitted fields are determined by expressions (21) and (22).

Using analytical expressions in [36] and the method for extracting polarizabilities introduced in [37], the dimensions of the inclusions were optimized.

Figure 8b shows numerically calculated amplitude and phase of transmittance through an infinite periodic array of the unit cells shown in Fig. 9a, the numerical calculations were performed using the HFSS package [38]. The simulations were carried out using periodic boundary conditions and simulating only the topology shown in Fig. 10.

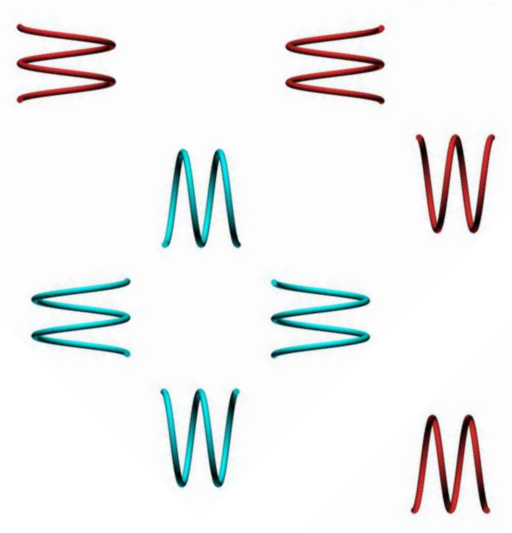

Figure 10: Simulated topology with periodic boundary conditions

The unit-cell dimensions in this example were chosen as follows: $D_1 = 14.14$ mm, $d_1 = 5$ mm. The helices have the pitch (the height of one turn) $l_{\text{ch}} = 1.38$ mm, and the radius of the turn $R_{\text{ch}} = 2.15$ mm. The radius of the inclusion wire is $r_0 = 0.33$ mm. As one can see from Fig. 8b, the transmittance is more than 88% at all frequencies, while the phase of transmission spans nearly full 2π range from 3.5 GHz to 5.5 GHz. In contrast to the theoretical results in Fig. 8a, in this case transmission is not unity at the resonance due to some dissipation of energy in copper helices.

As it was discussed in the previous section, the phase control of the transmitted waves can be accomplished by proportional scaling the inclusions dimensions. The phase variation is engineered, for simplicity, only along one direction, along the y-axis. In this design of transmitarrays with a non-uniform phase distribution the phase is tuned individually for each block of helices (not the entire unit cell) to ensure more smooth phase gradient over the transmitarray plane (see Fig. 9b). Using only one block of the unitcell is sufficient for constructing the array if it is put between two PEC boundaries on top and bottom, and the block handedness is alternated in the horizontal direction. According to the image theory, that setup ensures that the array is infinite vertically, and the whole unit cell is represented. Although in this case the chirality between adjacent blocks in the y-direction is not completely compensated (because the helices in the blocks have slightly different sizes and polarizability amplitudes), overall, the chirality effect is nearly suppressed due to a great number of different unit cells.

Based on the preceding theoretical analysis, a design of two transmitarrrays with

different functionalities is provided next, in order to demonstrate the potential of the approach. These examples show how to manipulate the direction of wave propagation as well as the wavefront shape.

3.1 Manipulating the Direction of Wave Propagation

In this example a design of a transmitarray that refracts normally incident waves (along the $-z$-direction) at an angle 45° in the yz-plane is presented. To achieve the effect of anomalous refraction, it is necessary to tune the inclusions dimensions in every block so that there is a linear phase gradient of transmission along the y-direction of the array. Thus, from the phased arrays theory, the array should be periodical along the y-direction with the period $d = \lambda / \sin 45° = 98.2$ mm, where λ is the wavelength at the operational frequency 4.32 GHz. The phase of transmission changes from 0 to 2π along one period d. The periodicity of the array in the x direction is $2D_1$ (the size of the unit cell), since along this direction there is no phase variation. In order to ensure smooth phase variations, maximal number of inclusion blocks is placed with the prescribed phases along the period d. Based on the dimensions of the helices (about $\lambda/12$), the period of six blocks of helices is built, i.e. $D_1 = d/6 = 16.4$ mm. In this example the spacing between the helices in the blocks $d_1 = 5.75$ mm. The dimensions of the helices in each block are listed in Table B1 in Appendix A.

The simulated results for the designed transmitarray are shown in Figures 11 and 12.

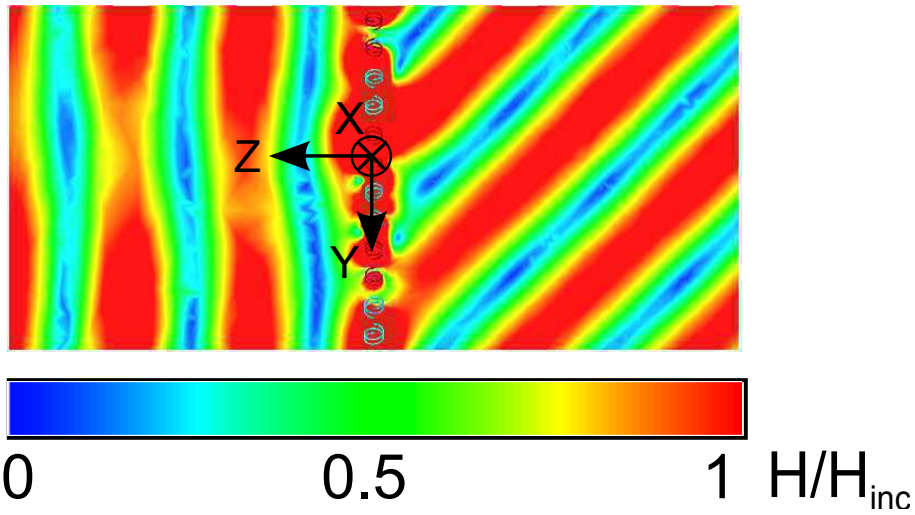

Figure 11: Magnetic field distribution normalized to the magnetic field of the incident wave. The incident wave propagates along the $-z$-direction with the electric field along the x-axis.

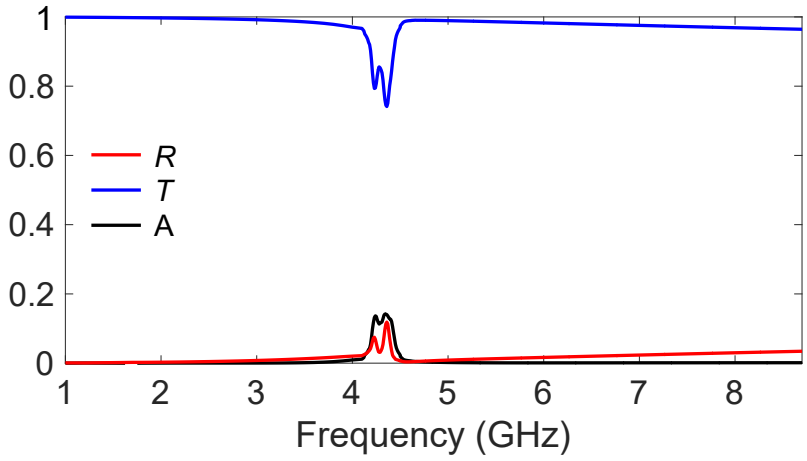

Figure 12: Reflectance R, Transmittance T, absorbance A, from the transmit array versus frequency.

Indeed, the structure refracts the incident wave at 45° from the normal. Figure 12 shows that at the operating frequency 4.32 GHz, the transmittance through the structure reaches 83%. Non-zero reflection of 5% and absorption of 12% in the transmitarray follow from the non-ideal impedance equalization [20]. Remarkably, the transmitarray passes through more than 95% of the incident power beyond its operational band from 4.13 to 4.47 GHz. At very high frequencies some parasitic reflections from the transmitarray appear. They are caused by the higher-order resonances in the sub-wavelength inclusions of the transmitarray and occur near the triple operating frequency at 13.2 GHz [3].

3.2 Wavefront Shaping

3.2.1 Simulations

In order to demonstrate the ability of wavefront shaping, a transmitarray that focuses normally incident plane waves in a line parallel to the x-axis is designed, numerically simulated, fabricated, and finally measured. Due to reciprocity, the metasurface, illuminated by a line source at the focal point, transmits a collimated beam. Such lens performance requires that the phase gradient of the transmitarray has a parabolic profile. The designed focal distance of the lens is just a fraction of the operational wavelength $f = 0.64\lambda$. Such a short focal distance is provided by the sub-wavelength sizes of the helices. The dimensions of the blocks of helices in this example are as follows: $D_1 = 14.14$ mm and $d_1 = 5$ mm. The lens is infinite along the x-axis with the periodicity equal to the size of one unit cell $2D_1$. Along the y-direction the lens is 410.1 mm long and contains 29 blocks of helices. The parabolic phase gradient is achieved due to precise tuning of the inclusions dimensions in each block (described in Table B2 in Appendix B) and dictated by

$$\phi_{\mathrm{t}}(y) = \phi_{\mathrm{t}}(0) + \frac{2\pi}{\lambda}\sqrt{y^2 + f^2}. \tag{33}$$

To test the performance of the designed lens, it is illuminated by a source of cylindrical waves located at the lens focal point. The simulation results at the operating frequency 3.9 GHz are presented in Fig. 13.

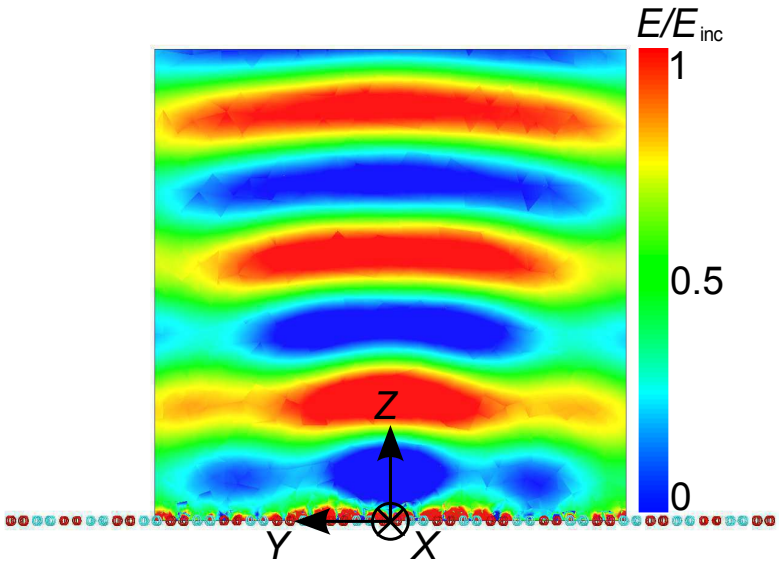

Figure 13: Simulated electric field distribution of the wave transmitted through the lens. The source of incident cylindrical waves is located in the focal point at $z = -f$. The lens center is at the origin of the coordinate system.

As expected, the lens transforms the cylindrical wavefront of the incident wave into a planar one.

3.2.2 Experiment

Next, experimental testing of the designed lens was conducted in a parallel-plate waveguide (Fig. 14).

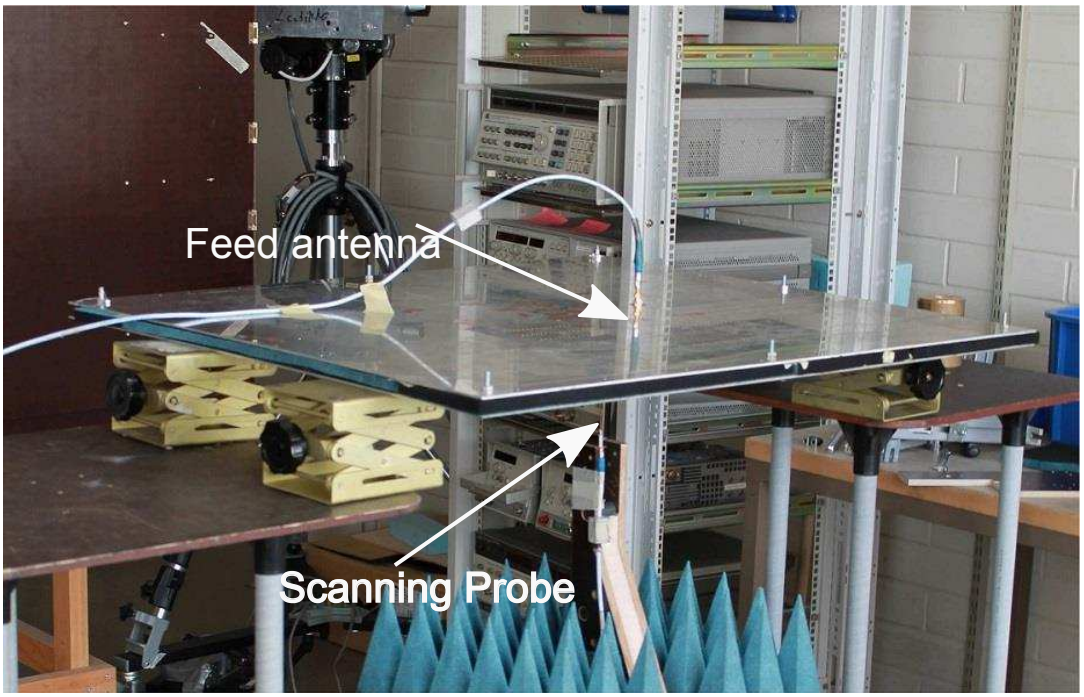

Figure 14: Experiment setup

According to the image theory, images of chiral inclusions placed between the plates of the waveguide represent equivalent chiral inclusions with the opposite handedness. Therefore, it is enough to place only one row of blocks (half of each unit cell) inside the waveguide (see Fig. 15). Effectively it emulates full unit cells (Fig. 9a) periodically repeated along the x-direction. The helical inclusions were fabricated trying to achieve precision of 0.01 mm, although they were handmade as it will be discussed later, the errors were acceptable and did not have much influence on the experimental results. The inclusions were then embedded in Rohacell-51HF material with $\epsilon_{\mathrm{r}} = 1.065$ and $\tan\delta = 0.0008$ for mechanical support. The parallel plate wave guide is of dimensions 90 cm$\times$80 cm and adjusted to the height of 14.14 mm which is the block period. The transmitarray was excited by a feed dipole antenna oriented along the x-axis and placed at the focal point at $z = -49$ mm. The bottom plate of the waveguide incorporates a 25 cm$\times$35 cm copper mesh with the period of 5 mm (see Fig. 15). Due to the deeply sub-wavelength periodicity, the mesh practically does not disturb the fields inside the waveguide. On the other hand, outside of the waveguide there are decaying fields in the near proximity of the mesh. The electric field distribution inside the waveguide can be analysed through these near fields measured using a small probe antenna (Fig. 14).

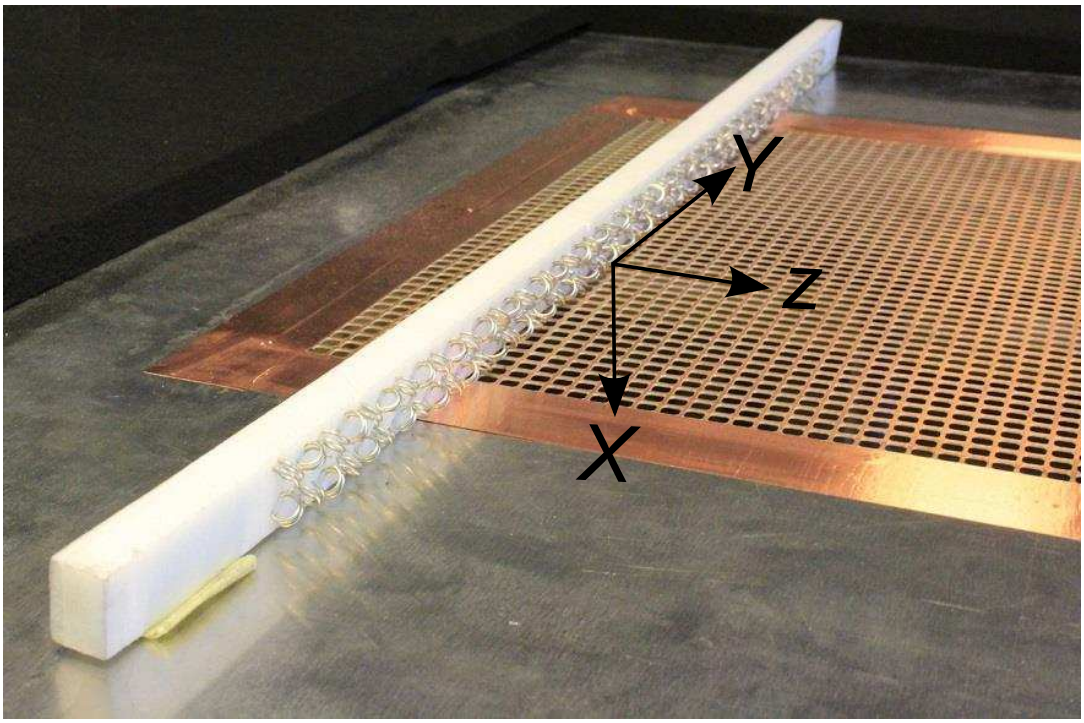

Figure 15: Fabricated metalens consisted of a single row of blocks

The feed antenna was connected to port 1 of Agilent Technologies E8363A vector network analyzer (VNA) and the scanning probe was connected to port 2. A field scanning system consisting of positioners controlled by a PC that moves in x and y directions holding the scanning probe was used to scan the near fields under the mesh. To illustrate, the field scanning system moves the scanning probe in the horizontal plane measuring the S_{21} at specific points and then sent to the VNA to construct the filed distribution.

The metalens was fabricated manually by wrapping wires with the specified lengths around screws with the specified dimensions to produce the required helices. The helices are made of 0.33 mm radius tinned copper wire according to the dimensions in Table B2. First the helices dimensions were taken from the simulated structure. According to those dimensions the helical length was calculated for each block of helices in the lens structure, then the wire was cut to the number of required helices having the predefined helical lengths. The minor diameters for the screws were then calculated, and the screws were ordered from a workshop according to the calculated dimensions. They were then tested by wrapping the cut wires around them and measuring the outer diameter of the wrapped helix to estimate the error. The error pattern was found to be uniform, so another patch was ordered with new dimensions that compensated that error. One of the screws is shown in Fig. 16.

Figure 16: Fabricated screw with the copper wire wrapped around it

The measured electric field distribution inside the waveguide at the resonance frequency 3.86 GHz is shown in Fig. 17.

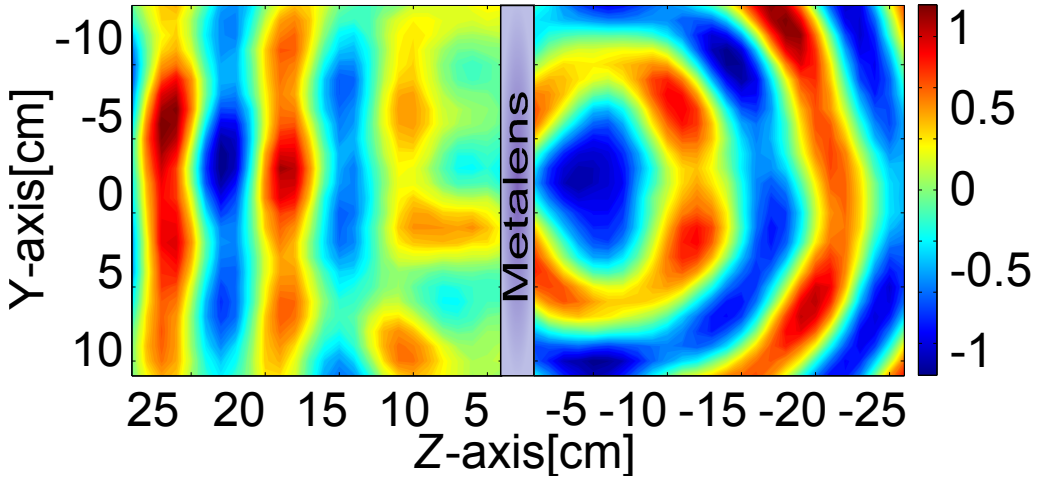

Figure 17: Distribution of the measured distribution of the x-component of the electric field inside the waveguide at the resonance frequency 3.86 GHz, the feed if located at the focal point of the metalens

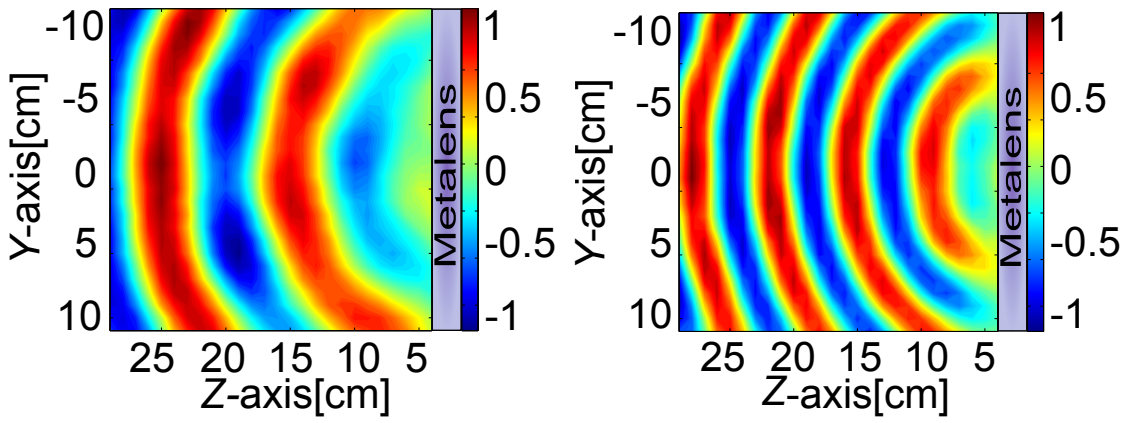

(a) (b)

Figure 18: Distribution of the measured distribution of the x-component of the electric field inside the waveguide: (a) at frequency 3 GHz and (b) at frequency 5 GHz. The feed antenna is located at point $z = -49$ mm. The lens location is shown by the blue box

One can see that the fabricated lens in fact transforms the cylindrical wavefront of the incident wave into a planar one. According to Fig. 18a and Fig. 18b, as expected, the lens does not interact with the incident waves beyond the operational band. Incident waves pass through the structure without attenuation and wavefront transformations. This experimental result confirms our theoretical findings.

4 Multifunctional Cascaded Metasurfaces

In this section the possibility for integration of the designed transmitarrays in a cascade of metasurfaces is explored. To highlight the three basic functionalities for wave control, such as manipulation of reflection, transmission and absorption properties, a composite structure consisting of three cascaded metasurfaces with the corresponding properties (see Fig. 19) is designed and numerically tested. Two versions of the composite are tested. The first version is with 0.3λ separation between its metasurfaces, while the second version is with 0.5λ separation, where λ is the wavelength at the highest operating frequency (6 GHz). The separations between the composite layers were chosen to reduce the near fields interactions, to ensure that at the highest operating frequency the whole composite thickness does not exceed one wavelength, and to ensure that the separation between the composite layers is larger than the separation between unit cells in each layer.

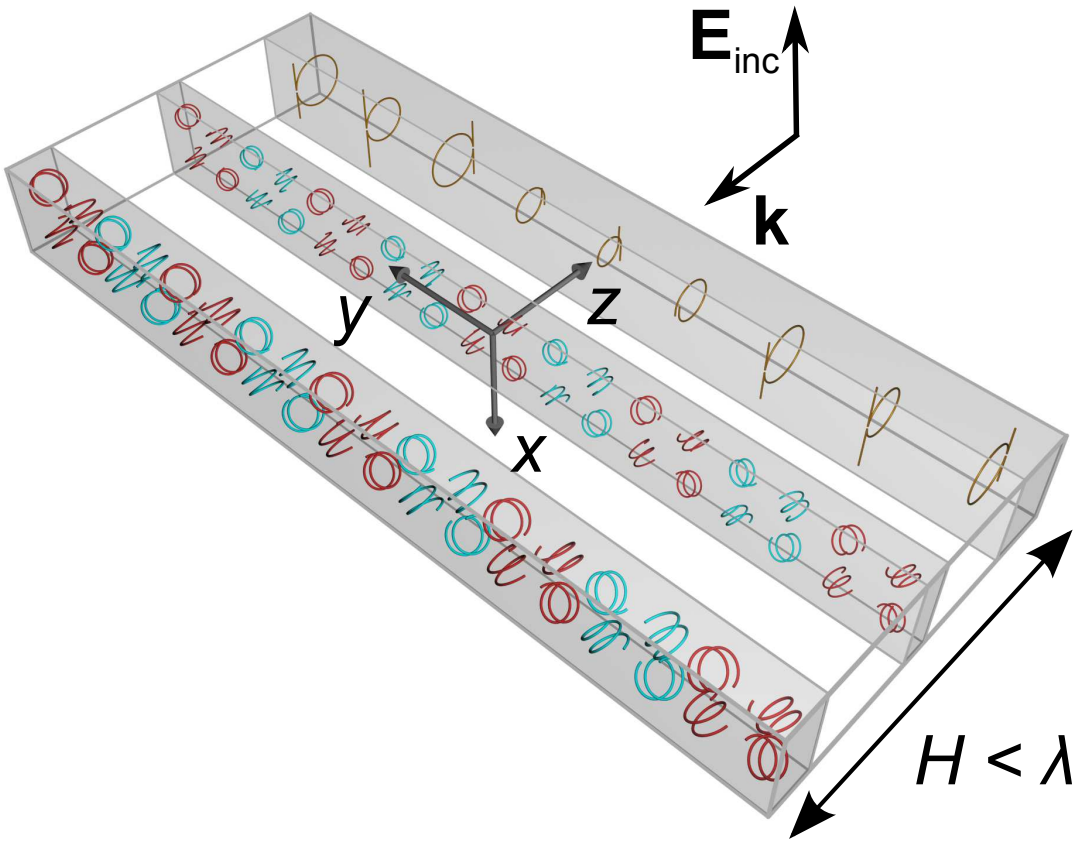

Figure 19: Multifunctional cascaded metasurface structure. The red color represents left handed helices and the blue color represents right handed helices

The incident wave illuminates the cascade normally from the $+z$-direction. The first metasurface illuminated by the incident wave is a so-called metamirror proposed in [1]. It nearly fully reflects normally incident waves at 5 GHz at an angle 45° from the normal. The second metasurface was designed to totally absorb incident radiation at 6 GHz. It represents a composite of double-turn helices similar to that described in [3] but tuned to operate at 6 GHz. All the helices in the absorber layer have equal dimensions: the helix pitch is $l_{\text{ch}} = 1.11$ mm, the helix radius $R_{\text{ch}} = 1.71$ mm and the wire radius $r_0 = 0.1$ mm. The helices are made of lossy nichrome NiCr60/15 with the conductivity about 10^6 S/m. The third cascaded metasurface is the lens designed in this thesis, operating at 3.9 GHz. All the metasurfaces consist of 29 blocks and have the same spacing 14.14 mm between the adjacent blocks.

The second (middle) metasurface is located at the origin of the coordinate system, while the first and the third metasurfaces are positioned at $z = 18$ mm and at $z = -23$ mm, respectively for the first version of the tested composite (with 0.3λ separation between its layers). For the second version of the composite (with 0.5λ separation between its layers) the locations of the first and third layers are $z = 30$ mm, and $z = -38$ mm, respectively. The overall thickness of the three-layer structure is $H = 48$ mm ($H = 75$ mm) for 0.3λ (0.5λ) versions of the composite, which does not exceed one wavelength at 6 GHz.

The performance of the metasurface cascade at the three operating frequencies for the first version is shown in Figs. 20c, 20e, and 21a, while for the second version with 0.5λ separation the performance is shown in Figs. 20d, 20f, and 21b. Figs. 20a, 20b, 21c, and 21d demonstrate the off-band transparency of the structures.

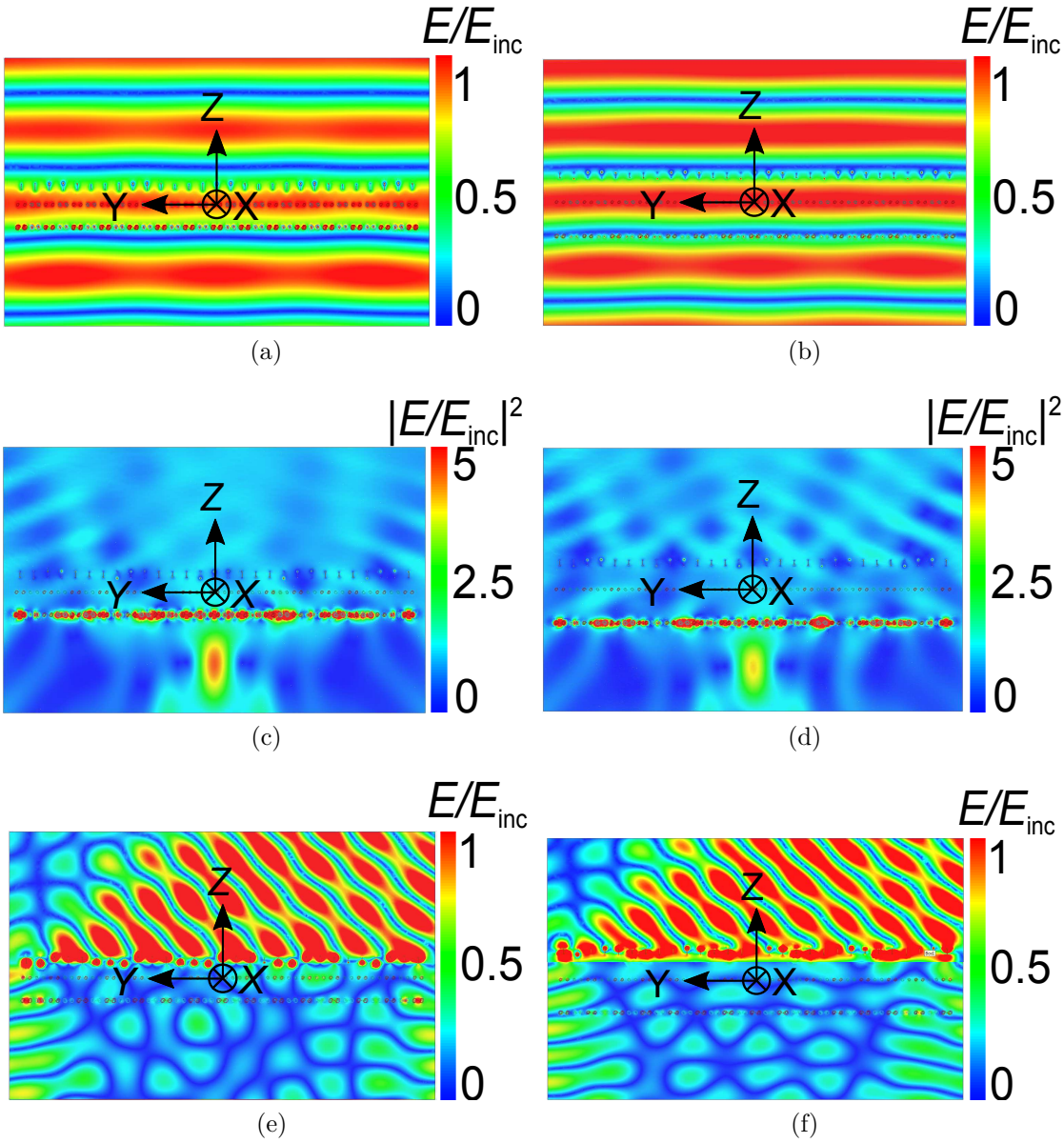

Figure 20: (a) and (b) Demonstration of the transparency of the structure at 2 GHz for 0.3λ and 0.5λ separations, respectively. (c) and (d) Cascade operation at 3.9 GHz for 0.3λ and 0.5λ separations, respectively. (e) and (f) Cascade operation at at 5 GHz for 0.3λ and 0.5λ separations, respectively.

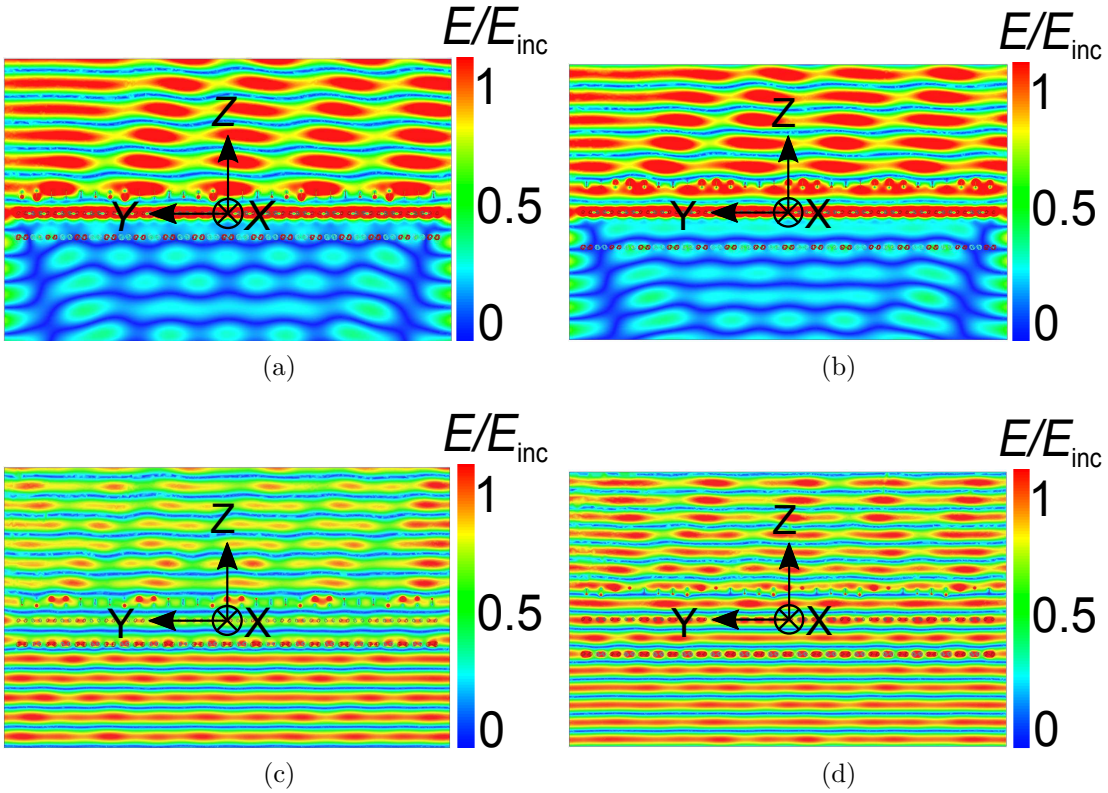

Figure 21: (a) and (b) Cascade operation at 6 GHz for 0.3λ and 0.5λ separations, respectively.(c) and (d) Demonstration of transparency of the cascade structure at 8 GHz for 0.3λ and 0.5λ separations respectively.

For the two tested structures at 5 GHz, incident waves are nearly totally reflected by the first metasurface at the angle 45° from the z-axis (Figs. 20c, and 20d). At 6 GHz, the first metasurface becomes "invisible" for incident waves, and nearly all the power is absorbed by the second metasurface (Fig. 20e, and 20f). Finally, incident waves at 3.9 GHz pass through the first two metasurfaces and are focused by the third metasurface (Fig. 21a, and 21b) nearly at the designed focal distance $f = 0.64\lambda$ for the structure with 0.3λ separation between its metasurfaces, while for the structure with 0.5λ separation $f = 0.46\lambda$. At 2 GHz and 8 GHz the whole structure is transparent, as shown in Fig. 20a, Fig. 21c for the structure with 0.3λ separation, and Figs. 20b and 21d for the structure with 0.5λ separation. This sub-wavelength three-layer composite is equivalent to the conceptual structure shown in Fig. 1c.

The data for reflection, transmission and absorption properties of the three-layer structure is summarized in Table 3 and Table 4 for the structures with 0.3λ and 0.5λ separations between their layers, respectively. Since the structure has a finite size, reflectance and transmittance were introduced as ratios of reflected and transmitted powers to the incident power calculated through the cross section of the metasurfaces.

As one can see from Tables 3 and 4, while reflection and absorption levels at 5 and 6 GHz, respectively, are high (more than 85%), transmission level at 3.9 GHz

Frequency, GHz	Transmittance T, %	Reflectance R, %	Absorbance A, %
2.0	99.6	0.2	0.2
3.0	96.8	3.0	0.2
3.9	59.2	26.8	14.0
5.0	8.0	85.8	8.3
6.0	7.9	5.1	86.5
7.0	84.3	12.5	3.2
8.0	84.6	10.7	4.7

Table 3: Numerically calculated characteristics of the cascaded structure with 0.3λ separation between its metasurfaces

Frequency, GHz	Transmittance T, %	Reflectance R, %	Absorbance A, %
2.0	99.4	0.2	0.4
3.0	98.7	0.6	0.7
3.9	53	34.8	12.2
5.0	6.4	88.1	5.5
6.0	9	4.1	86.9
7.0	87.6	8.4	4
8.0	84.1	11.6	4.3

Table 4: Numerically calculated characteristics of the cascaded structure with 0.5λ separation between its metasurfaces

is moderate (about 60%). This can be explained by two factors. First, there are some diffraction effects at the edges of the three finite-size metasurfaces. Second, the spectrum separation between the metasurfaces operating at 3.9 and 5 GHz is not high enough. The metamirror still reflects a small part of the incident energy at 3.9 GHz. As is seen from Table 3, far from the operating frequencies transmission of incident waves through the metasurface cascade exceeds 84%.

5 Conclusions

The study was set out to propose a new type of transmitarrays that allow full wave control (with the efficiency more than 80%) and are transparent beyond the operating frequency range. As a result of the frequency-selective response of such transmitarrays, they can be easily integrated in existing and new complexes of antennas and filters. They can also be integrated in multifunctional cascades of metasurfaces that preforms different functions at different frequencies while being transparent outside the operating frequency bands, which was the main inspiration of this thesis.

Conventional structures that manipulate electromagnetic waves in transmission were either not transparent outside of the operating frequency band such as antenna transmit arrays, or were broad band devices such as conventional light lenses and dielectric lenses, or even showed difficulties in the wave control like conventional aperture antennas.

Metamaterials was an interesting candidate for synthesizing the required transmitarrays, however, being volumetric leads to losses and relatively bulky size and difficulties in fabrication. That drove the attention to Huygens' metasurfaces, i.e. Thin layer 2D version of metamaterials that exhibit electric and magnetic induced dipole moments in each of its elements, which will lead to only forward scattering. However in literature, the structural elements of the previously designed transmitarrays using metasurfaces constitute reflectionless Huygens' sources only inside a narrow frequency band. Beyond this band reflections appear because of prevailing excitation of either electric or magnetic dipole. This is due to the fact that these elements have different frequency dispersions of the electric and magnetic dipole modes.

A theoretical analysis was then conducted to explore possible ways to synthesize the required transmitarrays using Huygens' metasurfaces. It resulted to the necessity of using single wire bi-anisotropic inclusions while compensating bi-anisotropy on the level of the unitcell.

Based on conducted theoretical analysis a refract array and a metalens were designed and numerically simulated. Moreover, the metalens was tested experimentally, and the results were very close to the simulations. Both structures showed high efficiency in transmission and were transparent outside the operating frequency band.

Finally the approach for designing multifunctional cascades of metasurfaces was verified by cascading the designed metalens with the absorber provided in [3] and the metamirror provided in [1], and the composite was numerically simulated. The composite showed the predefined functions at the required frequencies and was transparent outside the operating frequency bands. Despite the multifunctional response, the thickness of the designed structure is smaller than the operational wavelength. That approach of cascaded metasurfaces can be also extended to volumetric metamaterials.

The main challenge for implementing the designed structures are fabrication issues. However, hopefully in future work, the three-dimensional shape of the helical inclusions can be modified into an appropriate fabrication-friendly printed geometry.

References

[1] V. S. Asadchy, Y. Ra'di, J. Vehmas, and S. A. Tretyakov, "Functional metamirrors using bianisotropic elements", *Phys. Rev. Lett.*, vol. 114, no. 095503, Mar. 2015.

[2] V. S. Asadchy, M. Albooyeh, and S. A. Tretyakov, "Optical metamirror: all-dielectric frequency-selective mirror with fully controllable reflection phase", *J. Optical Soc. Amer. B*, vol. 33, no. 2, pp. A16-A20, Feb. 2016.

[3] V. S. Asadchy, I. A. Faniayeu, Y. Ra'di, S. A. Khakhomov, I. V. Semchenko, and S. A. Tretyakov, "Broadband reflectionless metasheets: Frequency-selective transmission and perfect absorption", *Phys. Rev. X*, vol. 5, no. 031005, July 2015.

[4] C. M. Segura, A. Dyke, H. Dyke, S. Haq, and Y. Hao, "Flat Luneburg lens via transformation optics for directive antenna applications", *IEEE Trans. Antennas Propagat.*, vol. 61, no. 12, pp. 1945-1953, Nov., 2013.

[5] S. Cornbleet, *Microwave Optics. The Optics of Microwave Antenna Design*, Academic Press, 1976.

[6] J. Huang and J. A. Encinar, *Reflectarray Antennas*, Wiley-IEEE Press, Nov. 2007.

[7] J. Shaker, M. R. Chaharmir, and J. Ethier, *Reflectarray Antennas Analysis, Design, Fabrication, and Measurement*, Norwood, Massachusetts, Artech House, 2013.

[8] Z. Popovic and A. Mortazawi, "Quasi-optical transmit/receive front ends", *IEEE Trans. Microw. Theory Tech.*, vol. 46, no. 11, pp. 1964–1975, Nov. 1998.

[9] S. V. Hum and J. Perruisseau-Carrier, "Reconfigurable reflectarrays and array lenses for dynamic antenna beam control: A review", *IEEE Trans. Antennas Propagat.*, vol. 62, no. 1, pp. 183–198, Jan. 2014.

[10] R. A. Shelby, D. R. Smith, and S. Schultz, "Experimental verification of a negative index of refraction", *Science*, vol. 292, no. 5514, pp. 77–79, Apr. 2001.

[11] A. Serdyukov, I. Semchenko, S. Tretyakov, and A. Sihvola, *Electromagnetics of Bi-anisotropic Materials Theory and Applications*, Amestredam, Netherlands, Gordon and Breach Science, 2001.

[12] N. Yu, P. Genevet, M. A. Kats, F. Aieta, J. -P. Tetienne, F. Capasso, and Z. Gaburro, "Light propagation with phase discontinuities: Generalized laws of reflection and refraction", *Science*, vol. 334, no. 6054, pp. 333–337, Oct. 2011.

[13] A. V. Kildishev, A. Boltasseva, and V. M. Shalaev, "Planar photonics with metasurfaces", *Science*, vol. 339, no. 6125, p. 1289, Mar. 2013.

[14] C. Pfeiffer and A. Grbic, "Metamaterial Huygens' surfaces: Tailoring wave fronts with reflectionless sheets", *Phys. Rev. Lett.,* vol. 110, no. 197401, May 2013.

[15] M. Selvanayagam and G. V. Eleftheriades, "Discontinuous electromagnetic fields using orthogonal electric and magnetic currents for wavefront manipulation", *Optics Express*, vol. 21, no. 12, pp. 14409–14429, June 2013.

[16] F. Monticone, N. M. Estakhri, and A. Alu, "Full control of nanoscale optical transmission with a composite metascreen", *Phys. Rev. Lett.,* vol. 110, no. 203903, May 2013.

[17] K. Achouri, M. A. Salem, and C. Caloz, "General metasurface synthesis based on susceptibility tensors", *IEEE Trans. Antennas Propagat.*, vol. 63, no. 7, pp. 2977–2991, July 2015.

[18] B. O. Zhu and Y. Feng, "Passive metasurface for reflectionless and arbitary control of electromagnetic wave transmission", *IEEE Trans. Antennas Propagat.*, vol. 63, no. 12, pp. 5500–5511, Dec. 2015.

[19] C. Pfeiffer and A. Grbic, "Millimeter-wave transmitarrays for wavefront and polarization control", *IEEE Trans. Microw. Theory Tech.*, vol. 61, no. 12, pp. 4407–4417, Dec. 2013.

[20] A. Epstein and G .V. Eleftheriades, "Passive lossless Huygens metasurfaces for conversion of arbitrary source field to directive radiation", *IEEE Trans. Antennas Propagat.*, vol. 62, no. 11, pp. 5680–5695, Nov. 2014.

[21] A. Epstein, and G. Eleftheriades, "Huygens' metasurfaces via the equivalence principle: Design and applications", *J. Optical Soc. Amer. B*, vol. 33, no. 2, pp. A31-A50, Feb. 2016.

[22] J. P. S. Wong, A. Epstein, and G. Eleftheriades, "Reflectionless wide-angle refracting metasurfaces", accepted for publication in *IEEE Antennas Wireless Propag. Lett.*, 2016.

[23] V. Asadchy, M. Albooyeh, S. Tcvetkova, Y. Ra'di, and S. A. Tretyakov, "Metasurfaces for perfect and full control of refraction and reflection," arXiv: 1603.07186.

[24] N. K. Grady, J. E. Heyes, D. R. Chowdhury, Y. Zeng, M. T. Reiten, A. K. Azad, A. J. Taylor, D. A. R. Dalvit, and H. -T. Chen, "Terahertz metamaterials for linear polarization conversion and anomalous refraction", *Science*, vol. 340, no. 6138, pp. 1304–1307, June 2013.

[25] T. Niemi, A. Karilainen, and S. A. Tretyakov, "Synthesis of polarization transformers", *IEEE Trans. Antennas Propagat.*, vol. 61, no. 6, pp. 3102–3111, June 2013.

[26] Y. Ra'di, V. S. Asadchy, and S. A. Tretyakov, "Total absorption of electromagnetic waves in ultimately thinlayers", *IEEE Trans. Antennas Propagat.*, vol. 61, no. 9, pp. 4606–4614, Sept. 2013.

[27] I. V. Semchenko, S. A. Khakhomov, and A. L. Samofalov, "Helices of optimal shape for nonreflecting covering", *Eur. Phys. J. Appl. Phys.*, vol. 49, no. 3, Mar. 2010.

[28] A. Balmakou, M. Podalov, S. Khakhomov, D. Stavenga, and I. Semchenko, "Ground-plane-less bidirectional terahertz absorber based on omega resonators", *Optics Letters*, vol. 40, no. 9, pp. 2084–2087, May 2015.

[29] D. R. Smith, W. J. Padilla, D. C. Vier, S. C. Nemat-Nasser, and S. Schultz, "Composite medium with simultaneously negative permeability and permittivity", *Phys. Rev. Lett.*, vol. 84, no. 18, p. 4184, May 2000.

[30] Y. Ra'di,V. S. Asadchy, and S. A. Tretyakov, "Tailoring reflections from thin composite metamirrors", *IEEE Trans. Antennas Propagat.*, vol. 62, no. 7, pp. 3749–3760, July 2014.

[31] S. A. Tretyakov, *Analytical Modeling in Applied Electromagnetics*, Norwood, Massachusetts, Artech House, 2003.

[32] M. Decker, I. Staude, M. Falkner, J. Dominguez, D. N. Neshev, I. Brener, T. Pertsch, and Y. S. Kivshar, "High-efficiency dielectric Huygens' surfaces", *Adv. Opt. Mater.*, vol. 3, no. 6, pp. 813–820, June 2015.

[33] J. K. Gansel, M. Thiel, M. S. Rill, M. Decker, K. Bade, V. Saile, G. Freymann, S. Linden, and M. Wegener, "Gold helix photonic metamaterial as broadband circular polarizer", *Science*, vol. 325, no. 5947, Sept. 2009.

[34] A. Radke, T. Gissibl, T. Klotzbücher, P. V. Braun, and H. Giessen, "Three-dimensional bichiral plasmonic crystals fabricated by direct laser writing and electroless silver plating", *Adv. Mater.*, vol. 23, no. 27 pp. 3018–3021, July 2011.

[35] V. S. Asadchy, I. A. Faniayeu, Y. Ra'di, I. V. Semchenko, and S. A. Khakhomov, "Optimal arrangement of smooth helices in uniaxial 2D-arrays", in *7th International Congress on Advanced Electromagnetic Materials in Microwaves and Optics – Metamaterials 2013*, Bordeaux, France, pp. 244–246, 2013.

[36] I. V. Semchenko, S. A. Khakhomov, and A. L. Samofalov, "Optimal helix shape: Equality of dielectric, magnetic, and chiral susceptibilities", *Russian Physics J.*, vol. 52, no. 5 pp. 473–479, 2009.

[37] V. S. Asadchy, I. A. Faniayeu, Y. Ra'di, and S. A. Tretyakov, "Determining polarizability tensors for an arbitrary small electromagnetic scatterer", *Photonics and Nanostructures - Fundamentals and Applicat.*, vol. 12, no. 4 pp. 299–304, Aug., 2014.

[38] ANSYS HFSS 2014: www.ansys.com/Products/Electronics/ANSYS-HFSS.

A Appendix 1. Parameters of 45° Refract Array

The 45° refracting transmitarray used in simulations consists of 6 blocks each of 4 identical inclusions made of 0.33 mm radius copper wire and oriented as shown in Fig. A1 where the red helices are left handed and the cyan ones are right handed.

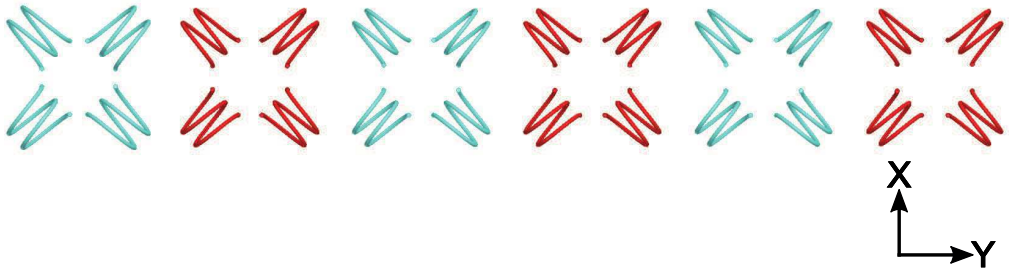

Figure A1: 45° refract array period

The pitch angle is 6.35° and the unit cell radius is 5.75 mm. The inclusions dimensions and their locations with respect to their position within the period are presented in Table A1.

Location of the block along the y-axis within the period d	Handedness of the helices in the block	Loop radius of the helices R_{ch}, mm	Pitch of the helices l_{ch}, mm	Phase of waves transmitted through the block
$-5d/12$	Left	2.34	1.63	$-\pi/3$
$-d/4$	Right	2.37	1.66	$-2\pi/3$
$-d/12$	Left	2.39	1.67	$-\pi$
$d/12$	Right	2.41	1.68	$-4\pi/3$
$d/4$	Left	2.44	1.71	$-5\pi/3$
$5d/12$	Right	2.70	1.88	-2π

Table A1: Dimensions of the helices in each of 6 blocks constituting period d

B Appendix 2. Parameters of Metalens

The metalens used in simulations and experiment consists of 29 unit cells with the same structure and the wire radius as the 45° refracting transmitarray. The pitch angle is 5.6° and the unit cell radius is 5 mm. The inclusions dimensions of only on half of the metalens starting from the center (middile) unit cell are presented in table B1, the dimensions are the same for the other half of the metalens due to the symmetry.

Distance from the center of the block to the center of the lens, mm	Handedness of the helices in the block	Loop radius of the helices R_{ch}, mm	Pitch of the helices l_{ch}, mm
0.0	Left	2.50	1.54
14.1	Right	2.48	1.53
28.3	Left	2.45	1.51
42.4	Right	2.43	1.50
56.6	Left	2.41	1.48
70.7	Right	2.38	1.46
84.8	Left	2.26	1.39
99.0	Right	2.59	1.60
113.1	Left	2.47	1.52
127.3	Right	2.43	1.50
141.4	Left	2.41	1.48
155.5	Right	2.36	1.46
169.7	Left	2.13	1.31
183.8	Right	2.52	1.55
198.0	Left	2.45	1.51

Table B1: Dimensions of the helices in each block of the lens

Table B2 represents the dimensions of the fabricated helices and the used screws. The minor diameter is the screw inner diameter and the ourter diameter is the diameter of the helix while it is wrapped around the screw.

Helix Diameter, mm	Minor Diameter, mm	Helical length, mm	Outer Diameter, mm	Pitch, mm	Handedness
5.00	3.68	31.57	5.66	1.54	Left
4.96	3.64	31.31	5.62	1.53	Right
4.90	3.58	30.94	5.56	1.51	Left
4.86	3.54	30.68	5.52	1.50	Right
4.82	3.50	30.43	5.48	1.48	Left
4.76	3.44	30.05	5.42	1.46	Right
4.52	3.20	28.54	5.18	1.39	Left
5.18	3.86	32.70	5.84	1.60	Right
4.94	3.62	31.19	5.60	1.52	Left
4.86	3.54	30.68	5.52	1.50	Right
4.82	3.50	30.43	5.48	1.48	Left
4.72	3.40	29.8	5.38	1.46	Right
4.26	2.94	26.89	4.92	1.31	Left
5.04	3.72	31.82	5.70	1.55	Right
4.90	3.58	30.94	5.56	1.51	Left

Table B2: Dimensions of the helices in each block of the fabricated lens, and the screw dimensions

C Appendix 3. Parameters of the Multifunctional Structure

Here the metamirror is the only layer presented as the rest of the layers dimensions were presented in previous sections. The metamirror consists of 6 omega inclusions repeated 5 times to fit the proposed 3 layer structure to perform the reflecting task. The last instance lacks one inclusion as we only have 29 unit cells for the transmit array and the absorber. Two types of omega inclusions are used and shown in the figure below.

The table C1 shows the position, dimensions and orientation of the metamirror inclusions.

Location along the y-axis within the period d	Type of an element	Loop radius, mm	Length of the straight wires, mm	Phase of the reflected wave	Orientation direction of the straight wires
-$d/4$	Ω	$R_2 = 3.43$	$l_2 = 3.49$	$4\pi/3$	$+z$
-$d/12$	Ω	$R_2 = 2.88$	$l_2 = 5.42$	π	$+z$
$d/12$	Ω	$R_2 = 3.35$	$l_2 = 4.01$	$2\pi/3$	-z
$d/4$	Twist.Ω	$R_1 = 3.01$	$l_1 = 1.00$	$\pi/3$	-z
$5d/12$	Twist.Ω	$R_1 = 2.28$	$l_1 = 2.84$	0	-z

Table C1: Dimensions of the metamirror's elements and their locations